JOURNAL OF GEOPHYSICAL RESEARCH, VOL. 115, D03202, doi:10.1029/2009JD012692, 2010

Click Here for Full Article

Online simulations of mineral dust aerosol distributions: Comparisons to NAMMA observations and sensitivity to dust emission parameterization

E. Nowottnick,[1] P. Colarco,[2] R. Ferrare,[3] G. Chen,[3] S. Ismail,[3] B. Anderson,[3] and E. Browell[3]

Received 18 June 2009; revised 28 August 2009; accepted 19 October 2009; published 4 February 2010.

[1] A key uncertainty within Earth system modeling lies in the parameterization of the emission process for mineral aerosols, where emission scheme choice can have implications for emitted dust fluxes. For our study, we include versions of dust emission schemes from the Goddard Chemistry, Aerosol, Radiation, and Transport (GOCART) and Dust Entrainment and Deposition (DEAD) models in the new NASA Goddard Earth Observing System version 4 model, to identify differences in simulated dust distributions caused by varying the emission scheme. The GOCART and DEAD schemes differ in their parameterization of the mobilization process, including their sensitivity to meteorological variables and the determination of the emitted particle size distribution. We focus on Saharan dust events during the NASA African Monsoon Multidisciplinary Analyses field campaign (August–September 2006) to compare with in situ, ground-based, and remote sensing observations. We find that the emission schemes produce comparable aerosol optical thickness and vertical extinction profiles, and their distributions compare well with observations from the space-based MODIS, OMI, MISR, and CALIPSO sensors, and the airborne LASE lidar. Neither emission scheme does especially well at capturing the variability or magnitude of specific dust events over the source region when compared to AERONET and MISR observations, but both improve downwind of the dust sources. Despite the similarities in the optical comparisons, the schemes differ in mass loadings owing to differences in their emitted dust particle size distributions over the source region. Our findings suggest that emission scheme choice for general circulation models is important only over the source region, where the emitted particle size distributions and corresponding mass budgets of emissions are influenced.

Citation: Nowottnick, E., P. Colarco, R. Ferrare, G. Chen, S. Ismail, B. Anderson, and E. Browell (2010), Online simulations of mineral dust aerosol distributions: Comparisons to NAMMA observations and sensitivity to dust emission parameterization, *J. Geophys. Res.*, *115*, D03202, doi:10.1029/2009JD012692.

1. Introduction

[2] Mineral dust aerosols play various roles in Earth's climate system, and remain a key source of uncertainty in assessing aerosol impacts on climate change [*Alley et al.*, 2007]. Dust directly influences the Earth radiation budget by scattering and absorbing solar and terrestrial radiation [*Sokolik and Toon*, 1996]. Regionally, the presence of dust can lead to a surface radiative forcing of -60 W m^{-2} (cooling) and up to 10 W m^{-2} (warming) within the dust layer, a net forcing that is comparable to clouds [*Sokolik and Toon*, 1996; *Tegen and Miller*, 1998; *Zhu et al.*, 2007]. Additionally, dust particles can serve as cloud condensation nuclei (CCN) [*Rosenfeld et al.*, 2001] or ice nuclei [*DeMott et al.*, 2003], thus modifying cloud properties and precipitation patterns [*Yoshioka et al.*, 2007], indirectly influencing Earth's climate system. Dust deposited to Earth's surface provides a source of iron to ecosystems in the Amazon and the Atlantic Ocean [*Falkowski et al.*, 1998, *Jickells et al.*, 2005]. Estimates of the anthropogenic influence on global dust concentrations are highly uncertain, and have been suggested to account for as much as 60% of the atmospheric dust load [*Mahowald and Luo*, 2003].

[3] Global aerosol transport models can be used as tools to gain insight into interactions of dust and the climate system. Global aerosol transport models have the advantage of high-spatiotemporal coverage, which complements ground-based or satellite data sets, where observations are frequently missing. Additionally, the processes in models are separable, so it is possible to isolate the contribution of dust relative to other aerosol species in the total aerosol load, which is difficult to determine from remote sensing

[1]Department of Atmospheric and Oceanic Sciences, University of Maryland, College Park, Maryland, USA.
[2]NASA Goddard Space Flight Center, Greenbelt, Maryland, USA.
[3]NASA Langley Research Center, Hampton, Virginia, USA.

Copyright 2010 by the American Geophysical Union.
0148-0227/10/2009JD012692$09.00

observations. The utility of this approach, though, is subject to our confidence in how well the model represents real atmospheric and aerosol processes. For example, despite the progress made in recent years in modeling the atmospheric dust aerosol cycle, there remain large discrepancies in dust mass budgets among the various models, and most models neglect possibly important processes (e.g., the indirect effects of dust aerosols on clouds) [*Zender et al.*, 2004]. Mass budget discrepancies can arise due to differences in dust source, sink, and transport processes, as well as treatment of dust microphysical processes (e.g., particle size distribution), making even estimations of the dust direct radiative forcing a difficult task [*Zender et al.*, 2004].

[4] In this study, we investigate dust aerosol distributions in a new global aerosol model. Dust aerosols are treated in the NASA Goddard Earth Observing System version 4 (GEOS-4) atmospheric general circulation model (AGCM) [*Bloom et al.*, 2005] with a version of the Goddard Chemistry, Aerosol, Radiation, and Transport (GOCART) model [*Chin et al.*, 2002] embedded as a component of GEOS-4 (P. Colarco et al., Online simulations of global aerosol distributions in the NASA GEOS-4 model and comparisons to satellite and ground-based aerosol optical depth, submitted to *Journal of Geophysical Research*, 2009). The GEOS-4 model differs from GOCART and similar offline chemical transport models (CTMs) in that the aerosol distributions are simulated entirely online within the system. That is, rather than having input meteorology specified at a particular frequency and then linearly interpolating in-between time steps, as is done in offline CTMs, GEOS-4 replays from a prior meteorological analysis by carrying out a short-term forecast until the availability of the next analysis increment (see section 2). This ensures an internal consistency in the model and aerosol state at all time steps, similar to a climate model, while still allowing the model to be constrained by real meteorological observations.

[5] To evaluate our simulated dust distributions, we chose to simulate the period of the NASA African Monsoon Multidisciplinary Analyses (NAMMA) field campaign (August–September 2006) and compare our results to aircraft in situ and remote sensing observations made during NAMMA, as well as remote sensing observations from the space-based MISR, MODIS-Aqua, OMI, and CALIOP instruments and ground-based observations from AERONET Sun-photometers in North Africa.

[6] Since a major uncertainty in dust models is with the treatment of dust sources, we consider two different dust emission schemes: the GOCART scheme based on *Ginoux et al.* [2001] and the Dust Entrainment and Deposition (DEAD) scheme from *Zender et al.* [2003]. There are two basic components to each of these schemes: a source function and a mobilization function. The source function is essentially a map of *possible* dust source regions based on some surface characteristics (e.g., soil type, topography) and specifies the efficiency with which a given surface can emit dust for a given set of meteorological parameters. The mobilization function relates the dust emissions to those various meteorological parameters (i.e., wind speed, soil moisture) and involves choices in how the physics of dust mobilization is parameterized. The dust emissions computed in the model are then the convolution of the source function and mobilization function.

[7] Previously, *Cakmur et al.* [2006] showed that for a single choice of mobilization function, simulated dust distributions are sensitive to a varying source function. On the other hand, *Luo et al.* [2003] showed that the choice of mobilization function influenced simulated dust concentrations, but their analysis was on longer climate scales and did not focus on specific events. *Colarco et al.* [2003] examined the role of source and mobilization function choice on downwind dust distributions during the Puerto Rico Dust Experiment, but did not unravel separately the effect of mobilization function for a given source function.

[8] In this study, we test the effects of the dust mobilization function choice on simulated dust distributions for the well-observed case study of dust transport during the NAMMA experiment. In our study, we hold the dust source function constant, using the topographical source function from *Ginoux et al.* [2001] (see section 3.2). This study builds upon *Colarco et al.* [2003] and *Luo et al.* [2003] by evaluating the mobilization function choice for a well-observed case study (NAMMA). To our knowledge, this is the first such study to do so with particular attention on the impact of mobilization function choice on dust vertical dust distributions, which we evaluate with airborne and space-based lidar observations.

[9] In section 2, we provide a description of the GEOS-4 model. In section 3, we introduce the GOCART and DEAD emission schemes and compare the underlying physics of each. In section 4, we present our simulated dust distributions and comparisons to various observational data sets. Our summary and conclusions are presented in section 5.

2. Model Description

[10] To explore the effects of dust emission schemes on dust distributions, we have been working with the NASA Global Modeling and Assimilation Office (GMAO) GEOS-4 AGCM [*Bloom et al.*, 2005]. GEOS-4 is based on the finite volume dynamical core [*Lin*, 2004] and contains physical parameterizations based on the National Center for Atmospheric Research (NCAR) Community Climate Model version 3 (CCM3) physics package [*Kiehl et al.*, 1996]. The land model used by GEOS-4 is version 2 of the Community Land Model Version 2 (CLM2) as described by *Bonan et al.* [2002]. GEOS-4 has the capability to run with horizontal resolution ranging from $4° \times 5°$ (latitude $\times$ longitude) to $1° \times 1.25°$ and either 32 or 55 vertical hybrid eta levels. GEOS-4 can be run in climate, data assimilation, or replay modes. In climate mode, the initial conditions are set and the model provides a forecast for a specified time period. In assimilation mode, the model is run similarly to climate mode, but a meteorological assimilation is performed every 6 h to adjust the model temperature, wind, and pressure fields. In replay mode, the model is replayed from a previous analysis. The replay is similar to how an offline CTM works, where dynamical fields are updated at specified time intervals. In contrast to an offline CTM, which interpolates the assimilated meteorological fields to the current model time step, the meteorology in the replay run is generated consistently within the GEOS-4 AGCM between updates from the assimilation. In this paper, GEOS-4 is run replaying from the GMAO GEOS-4 analyses [*Bloom et al.*, 2005].

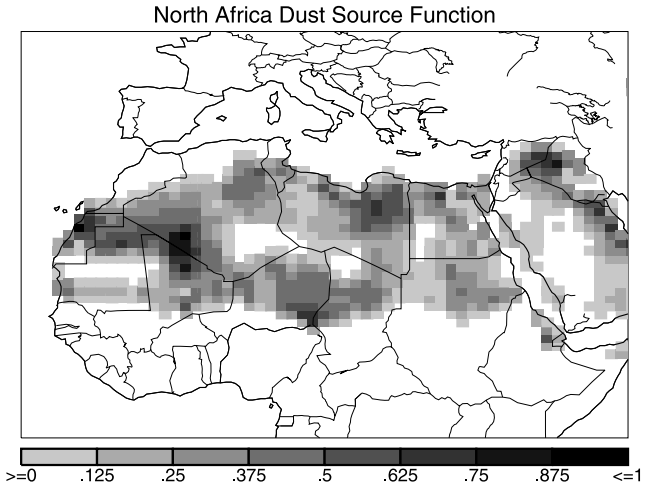

Figure 1. North Africa dust source function with AERONET site locations used in this study overlaid.

[11] The aerosol module used by GEOS-4 is based on GOCART [*Chin et al.*, 2002], which is embedded within GEOS-4 so that it runs consistently with the underlying AGCM. The aerosol module simulates five tropospheric aerosol species as passive tracers: dust, sea salt, black carbon, organic carbon, and sulfates. The implementation of the GOCART module in GEOS-4 and our application of it are as described by P. Colarco et al. (submitted manuscript, 2009), except as detailed in section 3 for the dust aerosols.

3. Dust Emission

3.1. Dust Emission and Entrainment on Earth

[12] Dust that is entrained into the atmosphere originates from erodible soil surfaces that are characteristically dry and free of vegetation. Natural dust sources primarily consist of topographic depressions that have accumulated alluvium during the Quaternary Period [*Prospero et al.*, 2002]. Accumulated particles can have a wide range of diameters, spanning from a few microns up to several millimeters [*Hillel*, 1982]. Large particles are too heavy to be lifted by typical surface winds, and the smallest particles are bound to the surface by cohesive forces. Particles with diameters nearly 100 μm are large enough for cohesive forces relative to the wind stress to be small, but are light enough to become mobilized into a bouncing motion along the surface called saltation [*Ivesen and White*, 1982]. During saltation, these particles are lifted several centimeters by the wind and fall quickly back to the surface due to gravity, creating a bouncing motion. Saltating particles impart their kinetic energy back to soil aggregates at the surface, displacing tiny fragments that were once immobile due to cohesive forces. This process is called "sandblasting," and it is the dominant mechanism for dust aerosol injection into the atmosphere [*Gomes et al.*, 1990].

3.2. Dust Emission in General Circulation Models

[13] The dust emission scheme for a global model requires (1) a dust source function to represent the location and relative erodibility of dust sources and (2) a parameterization of the mobilization process. Satellite observations are useful for detecting dust source regions. The dust source function used in this study is from *Ginoux et al.* [2001] and *Prospero et al.* [2002]. Global bare soil regions are identified as potential dust sources from a $1^\circ \times 1^\circ$ vegetation data set constructed from the advanced very high resolution radiometer (AVHRR) [*DeFries and Townshend*, 1994]. For each grid box, the efficiency for emitting dust is parameterized in terms of its local topography relative to surrounding grid boxes. That is, grid boxes that are in relative topographic depressions are assumed to have preferentially collected erodible sediments, and so are stronger dust sources than topographically elevated grid boxes. This approach has shown good consistency between the resulting global dust source function map (Figure 1) and dust aerosol locations observed with the Total Ozone Mapping Spectrometer (TOMS) aerosol index product [*Ginoux et al.*, 2001].

[14] For this study, we consider two different in situ parameterizations of the dust mobilization process applied to our model grid. The first is based on the current GOCART scheme, from *Ginoux et al.* [2001] (hereinafter referred to as the GOCART scheme). As an alternative, we have implemented a version of the DEAD scheme from *Zender et al.* [2003]. Both schemes parameterize dust emission in terms of the surface wind speed and distribute the emitted aerosol over a size distribution discretized by several size bins. Wind tunnel experiments have found that the horizontal flux of saltating soil particles is proportional to a power of the surface friction speed [*Ivesen and White*, 1982]. *Marticorena and Bergametti* [1995] developed a semiempirical parameterization for this relationship, accounting for the confounding effects of soil moisture and vegetative cover. Both the GOCART and DEAD schemes use this parameterization of the dry threshold wind speed, but they diverge at this point.

[15] In the GOCART scheme, the dry threshold wind speed is computed as a function of aerosol particle size according to the size bins chosen. This threshold is then modified to account for soil moisture, following *Ginoux et al.* [2001]. The emissions are then computed in terms of the 10 m wind speed so that emission occurs for each size bin only when the 10 m wind speed exceeds the threshold wind speed as determined in *Marticorena and Bergametti* [1995]. The equation for emissions is thus

$$F(r) = \begin{cases} C^*S^*s(r)^*U_{10\,\mathrm{m}}^2{}^*(U_{10\,\mathrm{m}} - U_\mathrm{t}(r,w)) & \text{if } U_{10\,\mathrm{m}} > U_\mathrm{t} \\ 0 & \text{otherwise} \end{cases}, \tag{1}$$

where $F(r)$ is the mass flux of aerosol emitted into a size bin of radius r, C is a tuning constant in units of kg s^2 m^{-5} used to set global dust emissions to a desired value, S is the spatially dust source function shown in Figure 1, $s(r)$ represents the efficiency of the soil at emitting particles of size r, $U_{10\ \mathrm{m}}$ is the 10 m wind speed, and U_t is the size-dependent threshold wind speed from *Marticorena and Bergametti* [1995] that has been modified for the presence of soil moisture w [after *Ginoux et al.*, 2001].

[16] By contrast, the DEAD scheme connects the threshold wind speed to the initiation of saltation rather than direct aerosol injection. Sandblasting caused by saltation is the main dust entrainment mechanism for sustained emission

[*Shao and Raupach*, 1993] and makes the emission physics of the DEAD scheme more satisfying. Unfortunately, determining soil grain saltation requires knowledge of the particle size distribution of the parent soil bed, which is not well known at global scales. For our implementation of DEAD, we follow *Zender et al.* [2003] by assuming that the parent soil contains a fixed monomodal soil particle size distribution of optimally sized particles ($D = 100$ μm, $u_t* = 0.209$ m s^{-1}) and compute the horizontal saltation flux of those. Therefore, the threshold formulation from *Marticorena and Bergametti* [1995] is used to determine the initiation of soil particle saltation as a function of surface properties and wind friction speed. The threshold is increased for soil moisture following *Fécan et al.* [1999], as well as to account for the loss of atmospheric momentum to nonerodible objects within the soil (e.g., rocks, vegetation), where we assume a fixed drag efficiency for all model grid cells, following *Marticorena and Bergametti* [1995]. The surface friction speed $u*$ is increased to account for the transfer of momentum to the surface from saltating particles, known as the Owen effect [*Gillette et al.*, 1998]. The aerosol mass injected is proportional to the horizontal saltation flux, which is computed in terms of the threshold wind speed and the wind friction speed (not the 10 m wind speed, as in the Ginoux scheme):

$$F(r)' = \begin{cases} C'*S*s(r)'*u^{*3}*\left(1-\frac{u_t^*(w)}{u^*}\right)\left(1+\frac{u_t^*(w)}{u^*}\right) & \text{when } \frac{u_t^*}{u^*} < 1.0 \\ 0 & \text{otherwise} \end{cases}, \tag{2}$$

where again $F(r)'$ is the mass flux of aerosol into a size bin of radius r, C' is a global tuning constant that also incorporates the efficiency with which the horizontal saltation flux translates to vertical aerosol mass flux, S is the same dust source function used in equation (1), $s(r)'$ is the aerosol particle size distribution, $u*$ is the surface friction speed from the land model that has been modified for soil moisture w.

[17] Comparing equations (1) and (2), we see that the dust emission flux in both schemes is approximately proportional to the third power of the wind speed for wind speeds exceeding some threshold. In the GOCART scheme, the relevant wind speed is the 10 m wind speed $U_{10\ \mathrm{m}}$, while in the DEAD scheme the relevant wind speed is the surface friction speed $u*$. We note that both schemes use the same threshold speed parameterization of *Marticorena and Bergametti* [1995], but apply it differently. The formulation in the GOCART scheme implies that $U_t = u_t*$, with modifications for soil moisture content. Although this is not strictly correct, it captures the observed behavior that higher surface wind speeds are needed to mobilize smaller aerosol particles. The parameterization in DEAD is more physically satisfying in that it explicitly accounts for saltation and sandblasting, but it is itself a simplification in that it neglects variability in soil particle size distributions, distributions of erodible surfaces within grid cells, and differences in the efficiency of horizontal-to-vertical mass flux transfer that depend on soil type. *Grini and Zender* [2004] modified DEAD to evaluate the effects of sub-grid-scale winds and different soil bed particle-size distributions, showing that these modifications affect simulated dust mass concentrations, optical depths, and the fraction of coarse particles, but not the timing of dust events. Unfortunately, the global variability of these properties is poorly known, particularly over the Saharan source region.

[18] For both emission schemes, we distribute the emitted aerosol mass across five transported size bins. On the basis of *Tegen and Lacis* [1996] and *Ginoux et al.* [2001], we choose the following radius bins: 0.1–1, 1–1.8, 1.8–3, 3–6, and 6–10 μm. The sub-bin particle size distribution of each bin follows from *Tegen and Lacis* [1996] in that we assume $d\mathrm{Mass}/(d\ln r) = \mathrm{constant}$. This determines an effective radius for each bin which is used in our emission and settling calculations: 0.73, 1.4, 2.4, 4.5, and 8 μm. Additionally, the first (smallest) size bin is further divided into four sub-bins for the purposes of optics, following *Tegen and Lacis* [1996]. For the GOCART scheme, the mass emitted to each bin is computed independently, based on how the wind speed exceeds the threshold for that bin. The soil particle size distribution enters as $s(r)$ as in equation (1) (following *Tegen and Fung* [1994]), where the mass of emitted clay particles ($0.1 < r < 1$ μm) is assumed to be one tenth of the total mass of emitted silt (particles of radius > 1 μm), that is $s = 0.1$ for the smallest bin. The four silt bins (1–1.8, 1.8–3, 3–6, and 6–10 μm) are each assigned a mass fraction of $s = 0.25$. We note that the emitted particle size distribution is dynamically determined in the GOCART scheme in that the threshold is computed for each size bin independently. In contrast, the DEAD scheme imposes a fixed trimodal lognormal distribution on the emitted aerosol that is based on the observed background dust particle size distributions near Saharan dust sources [*D'Almeida*, 1987].

[19] For both emission schemes, dust loss processes are parameterized in GEOS-4 following *Ginoux et al.* [2001] and *Chin et al.* [2002]. Dry deposition of dust particles by gravitational settling and turbulent mix-out is the dominant loss process, while wet deposition and convective scavenging become more significant after larger particles have fallen out during transport. Dust optical properties used in GOCART follow from the Global Aerosol Data Set [*Köpke et al.*, 1997].

[20] Table 1 summarizes the GOCART and DEAD emission schemes. Aside from the difference in winds used to parameterize the emission process, the major difference in the two schemes is that the emitted particle size distribution is fixed in the DEAD scheme, whereas it is dynamically generated in the GOCART scheme depending on the difference between the surface wind speed and the size-dependent threshold wind speed. However, because of how the threshold wind speed is applied in the GOCART scheme, the threshold speeds are generally much smaller than the 10 m wind speed ($U_t \ll U_{10\ \mathrm{m}}$), so that in practice there is little dynamical variation in the emitted size distribution. Both schemes have a drawback in that they are both in situ parameterizations that have been applied to a model grid. We use box-averaged parameters (i.e., wind speed and soil moisture) to represent the microscale processes that modulate dust emissions and cannot account for subgrid variability. Additionally, because both emission schemes have been applied to our model grid, global tuning constants are necessary to set the total global emissions. For

Table 1. Emission Scheme Comparison

	GOCART	DEAD
Source function	bare topographical depressions [*Ginoux et al.*, 2001]	bare topographical depressions [*Ginoux et al.*, 2001]
Dry emission threshold speed	wind tunnel experiments [*Marticorena and Bergametti*, 1995]	wind tunnel experiments [*Marticorena and Bergametti*, 1995]
Threshold speed modifications	soil moisture content [*Ginoux et al.*, 2001]	soil moisture content [*Fécan et al.*, 1999] and nonerodible objects [*Marticorena and Bergametti*, 1995]
Wind parameter used to determine emitted mass flux	10 m wind speed	surface friction speed
Flux equation [$F(r)$, $F(r)'$]	$F(r) = C * s(r) * u_{10\ \mathrm{m}}^2 * (u_{10\ \mathrm{m}} - u_{\mathrm{t}}(r, w))$ dynamic	$F(r)' = C' * S * s(r)' * u^{*3} * \left(1 - \frac{u_{\mathrm{t}}^*(w)}{u^*}\right)\left(1 + \frac{u_{\mathrm{t}}^*(w)}{u^*}\right)$ static
Size distribution	$s(r)$ [*Tegen and Fung*, 1994]	$s(r)'$ [*D'Almeida*, 1987]
Bin dependent mass fractions		
$r_{\mathrm{eff}} = 0.73\ \mu$m (0.1–1 μm)	0.1	0.112
$r_{\mathrm{eff}} = 1.4\ \mu$m (1–1.8 μm)	0.25	0.232
$r_{\mathrm{eff}} = 2.4\ \mu$m (1.8–3 μm)	0.25	0.296
$r_{\mathrm{eff}} = 4.5\ \mu$m (3–6 μm)	0.25	0.277
$r_{\mathrm{eff}} = 8\ \mu$m (6–10 μm)	0.25	0.064
Constants [C, C']	$C = 0.375 \times 10^{-9}$ kg s^2 m^{-5}	$C' = C'' * \alpha = 1.780 \times 10^{-5}$ kg s^2 m^{-5}, where $C'' = 3.716 \times 4$ kg s^2 m^{-5} and $\alpha = 0.0479$ is the sandblasting mass efficiency after assuming a globally uniform mass fraction of clay particles of 0.2

these simulations, GOCART emissions have been tuned to match the mass budget of emissions from *Ginoux et al.* [2001], which were shown to produce reasonable aerosol optical thickness (AOT) values as described by P. Colarco et al. (submitted manuscript, 2009). DEAD emissions were scaled so that the resultant regionally averaged AOT over North Africa was the same as the regionally averaged GOCART AOT over North Africa during the NAMMA period (August–September 2006).

4. Results

[21] From 19 August to 12 September 2006, the NAMMA field experiment was conducted from the Cape Verde Islands to help understand the evolution of African easterly waves, precipitation systems, and Saharan dust events over western Africa. Saharan dust events are primarily initiated by dry convection caused by intense solar heating [*Carlson and Prospero*, 1972; *Karyampudi et al.*, 1999]. Atmospheric mixing induced by dry convection leads to the formation of a deep boundary layer mixed with dust aerosol and can be transported over the Atlantic Ocean to the Caribbean as the Saharan air layer (SAL) [*Karyampudi et al.*, 1999; *Wong et al.*, 2009]. As solar intensity peaks during the Northern Hemisphere summer, thermal wind balance leads to the formation of the African Easterly Jet, which acts to transport the SAL westward on the north side of the jet axis [*Carlson and Prospero*, 1972; *Karyampudi et al.*, 1999]. NAMMA observations included 13 science flights made with the NASA DC-8 aircraft. We focus here on observations of the SAL obtained with lidar measurements of vertical structure [*Ismail et al.*, 2010] and in situ measurements of particle size distributions [*Clarke et al.*, 2007; *McNaughton et al.*, 2007; G. Chen et al., unpublished data, 2009] taken aboard the DC-8. In addition to the airborne observations of dust, we consider correlated observations from ground-based Sun photometers and several space-based remote-sensing platforms. We use these data sets to evaluate differences in our modeled dust distributions, and to compare the results of our two emission schemes.

[22] The model results presented below come from two sets of simulations of global aerosol distributions for the year 2006. In both simulations, the model was run at 1° × 1.25° horizontal resolution with 32 hybrid eta vertical levels (Table 2). The simulations are made in replay mode, driven by the GEOS-4 analysis products. Both simulations were run with the full complement of GOCART aerosols, but we vary the dust emission scheme in each. Thus, differences in simulated dust distributions can be directly attributed to the varying parameterizations of the dust emission process. To evaluate the performance of each emission scheme during the NAMMA period, dust distributions from both simulations are compared to the collection of observations during August and September.

4.1. GEOS-4 Emission and AOT Distributions Over North Africa

[23] Figure 2 shows the August–September average dust emissions and AOT at 550 nm for the GOCART and DEAD emission schemes. Displayed in the bottom left corner of each panel is the August–September average total dust emissions or mean AOT over North Africa, depending on the quantity of interest. The distinct difference between the emission schemes is that the DEAD emissions are more geographically sparse in their distribution over the continent than the GOCART emissions. GOCART emissions typically occur wherever the source function is greater than 0, because the 10 m wind speed can be an order of magnitude greater than the bin-dependent threshold speeds. Typical NAMMA August–September average 10 m wind speed values over the source region are about 3.5 m s^{-1}, while the GOCART size-dependent dry threshold speeds range from 2.45 m s^{-1} (smallest transport bin) to 0.41 m s^{-1} (largest transport bin). In contrast, because typical August–September average surface friction speed and the dry threshold speed are comparable in magnitude (about 0.23 m s^{-1}), the spatial distribution of DEAD emissions is sparse, and the occur-

Table 2. Typical GEOS 4 Vertical Resolution Over the Tropical North Atlantic Ocean

Model Level	Midlayer Altitude (km)
1	0.06
2	0.27
3	0.65
4	1.26
5	2.09
6	3.15
7	4.39
8	5.69
9	6.96
10	8.20
11	9.39
12	10.53
13	11.62
14	12.68
15	13.69
16	14.68
17	15.64
18	16.60
19	17.55
20	18.54
21	19.60
22	20.74
23	22.00
24	23.41
25	25.07
26	27.06
27	29.40
28	32.14
29	35.37
30	39.30
31	44.27
32	50.57

rence of emission events is more likely to be modulated by the presence of soil moisture. The GOCART scheme emits a greater average mass of dust (91 Tg) when compared to DEAD (54 Tg) during the NAMMA period. We recall that the magnitude of emissions in each scheme was tuned to yield a comparable, regional-average AOT (τ_{550} = 0.14, Figure 2) that is consistent with P. Colarco et al. (submitted manuscript, 2009).

[24] Despite the large difference in the emission magnitude, the same regional AOT value is obtained because the two schemes emit particles of different sizes, with differing optical efficiencies. Figures 3a and 3b show the August–September averaged values of size-dependent dust emissions (solid), dry deposition (dashed), and the fractional dust AOT contribution over North Africa. The GOCART scheme emits a greater mass of particles than the DEAD scheme in all, but the first size bin. This is a consequence of how the threshold equation is applied to determine direct aerosol injection in the GOCART scheme instead of to determine the initiation of saltation as in the DEAD scheme. Here the threshold wind speed is relatively low for large particles (bins 4 and 5). However, these large particles settle quickly from the atmosphere (as evidenced by the high dry deposition values) and have little contribution to the total AOT. In contrast, in the DEAD scheme the threshold equation determines the onset of saltation, and a static aerosol particle size distribution is assumed such that the peak aerosol emission occurs in the third transport bin (see Table 1). Similar to the GOCART scheme, the fifth transport bin has comparable values of emissions and dry deposition, implying that nearly all emitted particles at this size are removed rapidly. The DEAD scheme emits relatively more particles in the first transport size bin. Figure 3b shows how this corresponds to a larger contribution to the total dust AOT from these particles than in the GOCART scheme, and is the explanation for the comparable regional AOT values obtained despite the large difference in the emitted aerosol mass.

4.2. Aerosol Optical Thickness

[25] To help validate simulated spatiotemporal dust distributions using the GOCART and DEAD emission schemes during NAMMA, we compare our simulations to measurements of AOT from the spaceborne MISR instrument and ground-based AERONET Sun photometers.

4.2.1. Multiangle Imaging Spectroradiometer

[26] The multiangle imaging spectroradiometer (MISR) was launched on NASA's Terra satellite on 18 December 1999 [*Kahn et al.*, 2005]. MISR contains nine push-broom cameras to observe the same point on Earth from nine different angles (nadir, ±26.1°, ±45.6°, ±60.0°, and ±70.5°) and in four spectral bands (446, 558, 672, and 866 nm). Aerosol retrievals are performed using a look-up table approach with retrievals provided at 17.6 × 17.6 km^2 horizontal resolution, where constraint of angular information from the multiangle viewing geometry is used to characterize the aerosols and also permits retrievals over bright surfaces [*Diner et al.*, 1998; *Abdou et al.*, 2005]. The MISR swath width along the ground is at least 360 km, providing global coverage approximately every 9 days. We aggregate the MISR Level 2 AOT at 558 nm to our model grid. We use the latest version of the MISR aerosol retrieval algorithm (v. F12_0022).

[27] Figure 4 shows monthly mean MISR (555 nm), GEOS-4 GOCART (550 nm), and GEOS-4 DEAD (550 nm) AOT from all aerosols during August and September. For a consistent comparison, GEOS-4 AOT values have been sampled from grid cells at the synoptic time nearest the MISR retrieval. On each plot, white areas correspond to regions where MISR was unable make any retrieval at all (e.g., due to clouds) and therefore we also did not sample the model. In August, MISR reports moderate AOT values (~0.6) over most of the southern Saharan desert, with two AOT hot spots (>1.0) over Mauritania and Mali (box 1) and Lake Chad (box 2). Over the tropical North Atlantic Ocean, AOT values are moderate off the coastline, but drop off quickly west of 30 W (box 3). In comparison, both GEOS-4 simulations have AOT values that are 30–50% less than MISR over the southern Saharan desert and at least 50% less over the hot spots (boxes 1 and 2). Just off the coastline, GEOS-4 AOT magnitudes are comparable to MISR, but drop off more quickly toward the west near 22.5 W (box 3). Over the tropical North Atlantic Ocean, the MISR dust plume extends all the way to the Caribbean, while both GEOS-4 plumes are not as pronounced. Comparing the GEOS-4 simulations, both emission schemes simulate comparable AOT distributions of North Africa, with the GOCART scheme matching MISR better over Mauritania and Mali (box 1) and the DEAD scheme having slightly better agreement with MISR over the Lake Chad region (box 2). During September, MISR retrieves moderate AOT values (~0.6) over the southern Saharan desert again, but only has one hot

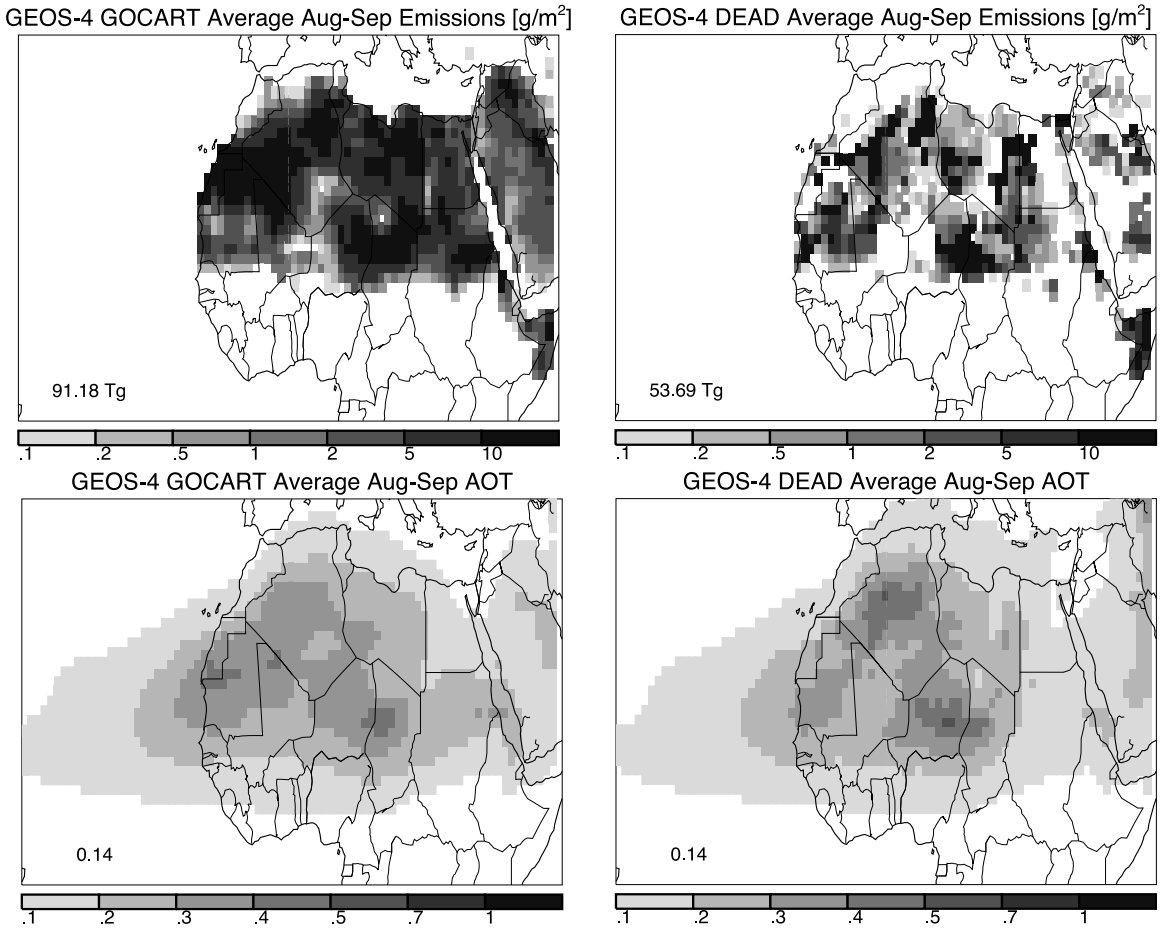

Figure 2. August–September (top) average emissions and (bottom) AOT for (left) GEOS-4 GOCART and (right) GEOS-4 DEAD emission schemes. Total region emissions (Tg) and average AOT are displayed in the bottom left of each plot.

spot over Lake Chad (box 2). Over the tropical North Atlantic Ocean in September, MISR shows somewhat lower AOT near the African coast than in August. In both months, MISR shows long-range transport of high dust AOT into the western Atlantic and Caribbean. Although the dust transport appears to carry further west in August, the peak of the AOT is higher (~0.4–0.5) and appears further west (at about 50°W) than in August (box 3). The model captures the lower values near the coastline, but not the apparent extended long-range transport in September. Comparison of the MISR observations to the Moderate Resolution Imaging Spectroradiometer (MODIS) Aqua AOT (not shown) suggests that the pattern of transport MISR shows in September is somewhat a sampling artifact. The MODIS observations provide daily near-global AOT retrievals, compared to the MISR narrower swath observations, which obtain global coverage approximately every 9 days. In short, the MISR observations emphasize a particular event that the model underestimated the intensity of. Over North Africa, both GEOS-4 simulations produce AOT distributions that are more comparable in magnitude to one another than to MISR. Both schemes simulate maximum AOT values over the Lake Chad region, where the DEAD scheme is more comparable with MISR (box 2). Again, both schemes simulate AOT values that are 50% less than values retrieved by MISR over Mauritania and Mali (box 1). Over the tropical North Atlantic Ocean, neither scheme captures the magnitude and westward extent of the MISR dust plume over the tropical North Atlantic Ocean (box 3).

[28] In Figure 5, we show the day-to-day variation of the MISR and simulated AOT as averaged within each of the three boxes illustrated in Figure 4. When compared to MISR, both model simulations consistently underestimate the magnitude of AOT in all three boxes. The coefficient of determination correlation (R^2) of the model and MISR AOT is worst for both simulations in the region of Lake Chad (box 2: GOCART R^2 = 0.058, DEAD R^2 = 0.259). Correlation is more modest over Mail and Mauritania (box 1: GOCART R^2 = 0.410, DEAD R^2 = 0.395) and also over the Tropical North Atlantic (box 3: GOCART R^2 = 0.560, DEAD R^2 = 0.377). It is evident that the model has difficulty with the timing of dust events over Lake Chad, but improves downwind. While box 1 correlates moderately well with MISR, both simulations underestimate the AOT magnitude by nearly 50% throughout August. The simulations compare best over the Tropical Atlantic Ocean (box 3) where AOT magnitudes are most similar to MISR and have modest correlations.

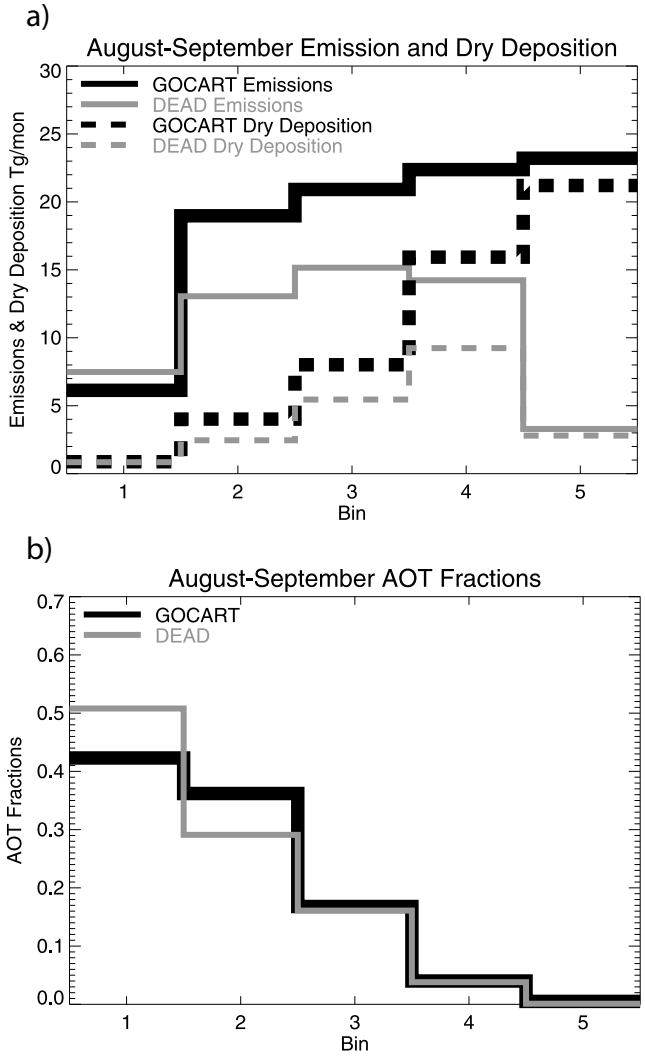

Figure 3. (a) August–September average total emissions (solid), total dry deposition (dashed). (b) August–September average fraction of dust AOT for each transport bin over North African for the GOCART (black) and DEAD (gray) emission schemes.

4.2.2. Operated Aerosol Robotic Network

[29] We compare our simulated values of AOT to observations from the NASA operated aerosol robotic network (AERONET) of global, ground-based Sun photometers. AERONET measures direct solar beam extinction every 15 min at 340, 380, 440, 500, 670, 870, and 1020 nm, providing AOT values at 440, 670, 870, and 1020 nm with an accuracy of ±0.015 [*Holben et al.*, 2001]. Principle plane and almuncantar scans provide sky radiance information used to invert aerosol properties to obtain size distributions and fine mode fractions of the AOD [*Dubovik and King*, 2000]. We use the Version 2 cloud-screened and quality-assured (Level 2) [*Smirnov et al.*, 2000] daily averaged AERONET AOT data for comparison to our simulations during August and September. GEOS-4 to AERONET comparisons are made by sampling the AOT from all species from the model grid box ($\sim$100 $\times$ 100 km^2) that contains the AERONET site. To obtain AERONET AOT at 550 nm, we used the Angstrom parameter α, defined by

$$\tau_1 = \tau_2 \left(\frac{\lambda_1}{\lambda_2}\right)^{-\alpha}, \tag{3}$$

where τ_1 and τ_2 are initially the AOT values reported at λ_1 = 440 nm and λ_2 = 870 nm, respectively. The Angstrom parameter is used to measure the wavelength dependence of AOT. Once the Angstrom exponent is known, equation (3) may be used to derive τ_{550} following using τ at either $\lambda = 440$ nm and λ = 870 nm.

[30] Four AERONET sites are located near the dust source regions in North Africa during the NAMMA period (Figure 1). Sites were chose based on their proximity to the source region and availability during the NAMMA period. Figure 6 compares daily averaged GEOS-4 GOCART and DEAD AOT values from all aerosols to AERONET. For each site, the mean AOT for AERONET, GOCART, and DEAD on days when AERONET provides retrievals is displayed in the upper left corner and the coefficient of determination (R^2) correlation of the AERONET AOT time series with GOCART and DEAD is displayed in the upper right corner. In general, the two model simulations are well correlated with each other. At Tamanrasset-TMP (within the large-scale dust source regions), we have a generally low correlation between the model AOT and the AERONET observations (GOCART R^2 = 0.278, DEAD R^2 = 0.333). Both simulations fail to capture dust events that occur on 8/10, 8/15, and 8/28, artificially simulate a dust event from 9/21 to 9/24, but are able to accurately capture a dust event that occurred from 9/2 to 9/5. These results are consistent with MISR in that the model has difficulty with the timing of dust events near the source region.

[31] Dakar and Banizoumbou are sites peripheral to the dust source region. Similar to Tamanrasset, the mean AOT is comparable between the model simulations and the AERONET observations at both sites. At Dakar, AERONET reports high AOT values from 8/15–8/20, 8/25, 9/5–9/9, and 9/21, whereas GEOS-4 values are never higher than 0.7. Despite the differences in magnitude, the timing of GEOS-4 AOT events has moderate agreement with AERONET (GOCART R^2 = 0.454, DEAD R^2 = 0.387). At Banizoumbou, there is poor agreement between AERONET and GEOS-4 AOT time records (GOCART R^2 = 0.101, DEAD R^2 = 0.018). Often there is a lag between simulated and observed AOT values (e.g., 8/20–8/25), which result in low correlation coefficients.

[32] Santa Cruz, Tenerife, is downwind of the dust source region and AOT magnitudes are correspondingly lower, yet the periodic passing of dust events is evident. Here there is relatively high correlation in the timing of events between the model and the observations (GOCART R^2 = 0.583, DEAD R^2 = 0.644), but mean AOT values are somewhat higher in the model than in the observations.

[33] Our simulations have their greatest correlation with AERONET observations downwind of the source region (Santa Cruz, Tenerife), have moderate agreement near the source region at the Tamanrasset-TMP site and peripheral site Dakar, and poor agreement at Banizoumbou. Over the source region, meteorological observations to constrain the

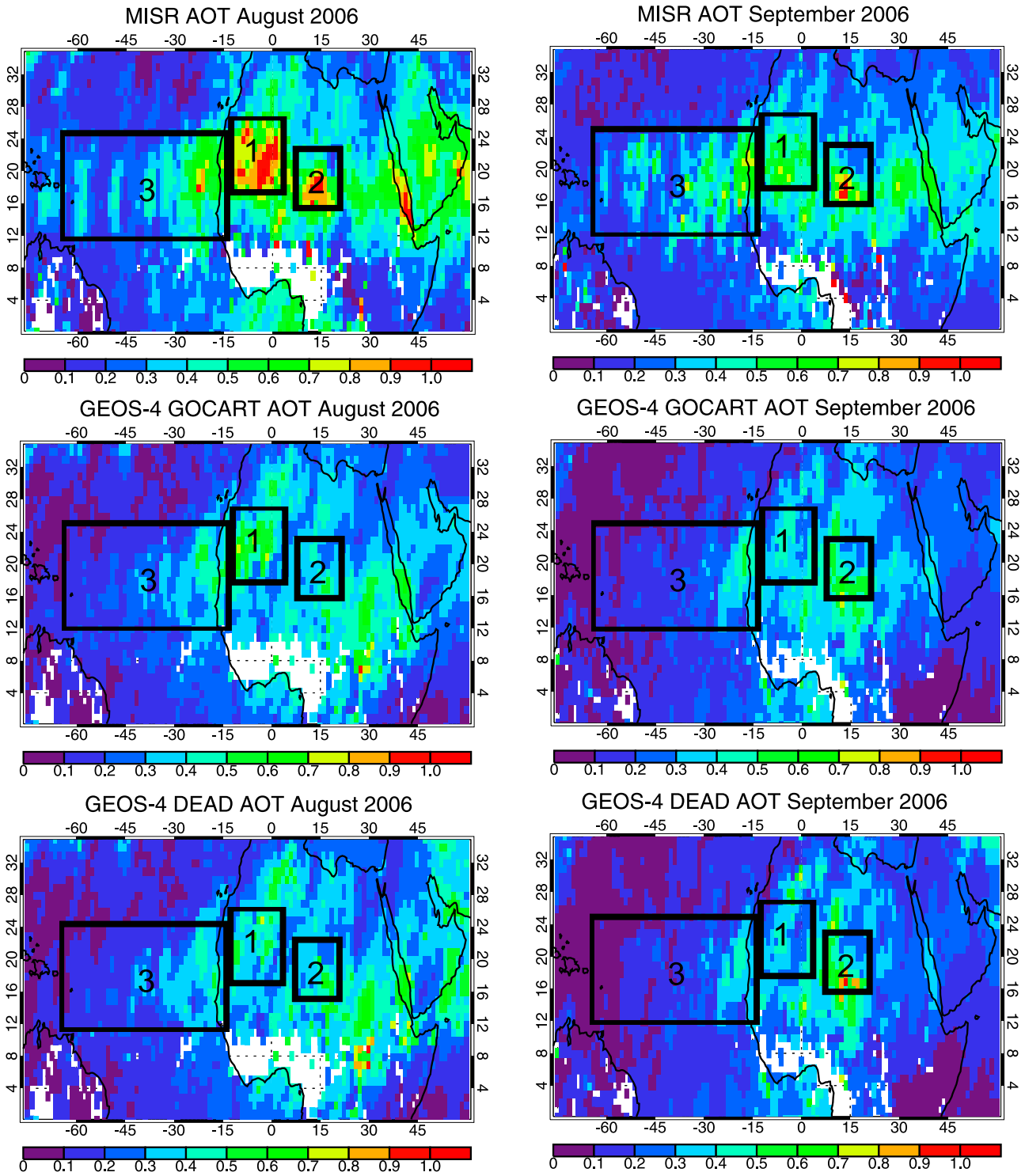

Figure 4. (top) MISR AOT, (middle) GEOS-4 GOCART AOT, and (bottom) GEOS-4 DEAD AOT during (left) August and (right) September. Boxes 1–3 are regions of interest for model evaluation.

model are scare, so the wind fields that drive the dust emissions are based on the model physics more than on observations. Further from the dust sources, however, it is generally the case that more meteorological observations are available for assimilation into the analyses driving the model, and hence the simulated loadings have better agreement with the observations. Additionally, although we acknowledge limitations in the dust emissions schemes, errors in accurately simulating other aerosol types will play a role in the overall fidelity of the simulated AOT with observations. In particular, at Dakar and Banizoumbou inspection of the Angstrom parameter determined from AERONET observations suggests that some significant aerosol events are due to aerosols other than dust (not

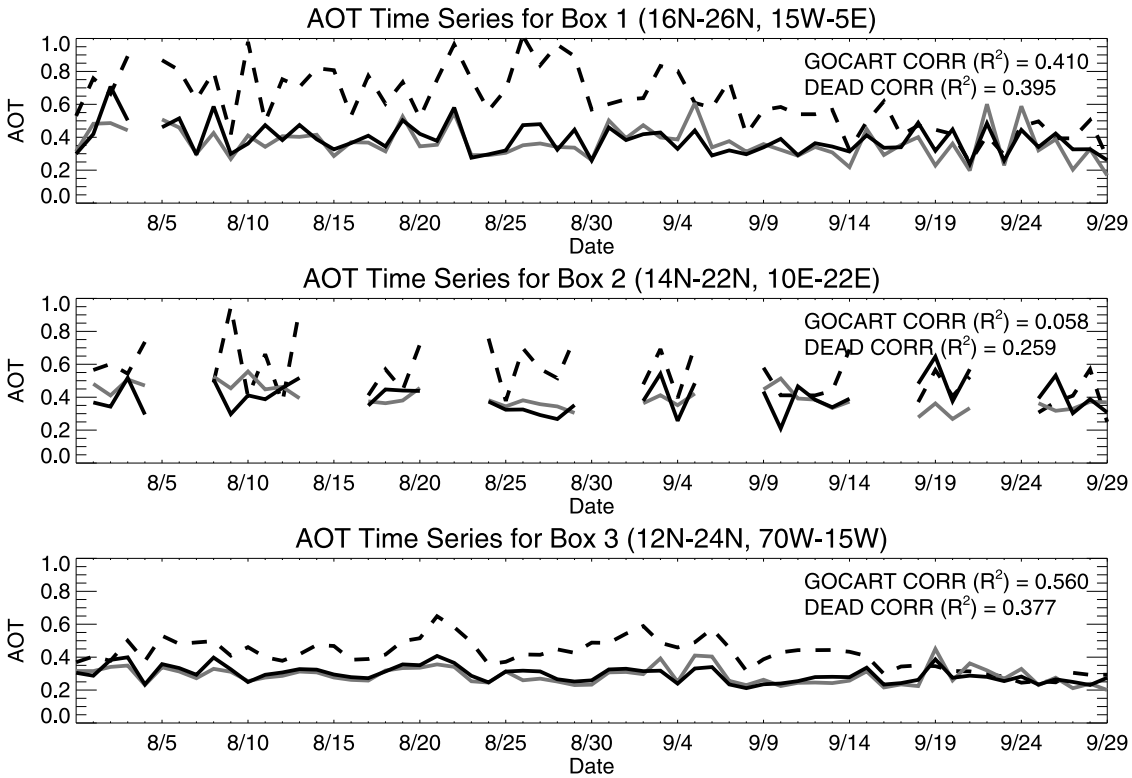

Figure 5. MISR (dashed) and sampled GOCART (black) and DEAD (gray) daily AOT for boxes 1–3. Coefficients of determinations are displayed in the top right.

shown). Alternatively, errors in the timing of events may be attributed to either model spatial scale or (and related) transport errors. We recall that the AERONET observations are essentially point measurements, while the model grid boxes are approximately 100 × 100 km^2 in size. Therefore, the model cannot resolve sub-grid-scale plume that may be driving the AERONET observations. This explanation is plausible, as we made this comparison to AERONET observations again by averaging the model over the nine grid boxes encompassing and surrounding the AERONET site (so considering a box of approximately 300 × 300 km^2 area) and achieved essentially the same results at all four sites (not shown). Therefore, the differences between the model and observations are not simply the result of plume misplacement, but either reflect real errors in the model aerosol composition or missing sub-grid-scale aerosol plumes. Mean AOT comparisons to AERONET are consistent with MISR in that both GEOS-4 simulations have better agreement with one another than with the observations during August and September. However, unlike comparisons to MISR, mean simulated AOT values are not consistently low when compared to AERONET. We see that mean AOT values are very comparable to AERONET at Dakar, have good agreement at Tamanrasset-TMP (DEAD) and Banizoumbou (GOCART), and are slightly biased high at Santa Cruz Tenerife.

4.3. Particle Size Distributions

[34] We evaluate the modeled dust particle size distribution in the context of observations from AERONET and airborne measurements. Recall that the initial particle size distribution is dynamically generated for simulations with the GOCART emissions (wind speed dependent) but is prescribed for simulations with the DEAD emission scheme. For both schemes, however, we recall that the particle size distribution evolves during transport as particles are removed by dry and wet removal processes.

4.3.1. AERONET

[35] To measure the ability of each emission scheme to simulate dust particle size distributions, simulated size distributions were compared to those retrieved at the Tamanrasset-TMP, Santa Cruz Tenerife, Dakar, and Banizoumbou AERONET sites (Figure 1). Here we compare only the simulated dust particle distribution of the AERONET retrievals. At each site during August and September, the daily averaged AERONET size distributions are constructed from observations where the AOT is greater than 0.4 at 440 nm [*Dubovik and King*, 2000]. From these, we construct a mean size distribution for the August–September period at each site. The simulated particle size distributions were computed at each vertical level in the model from the simulated mass distributions, and the values were integrated in the vertical to produce a column-integrated volume distribution, consistent with the AERONET retrieval.

[36] Shown in Figure 7 is mean August to September volume distributions for AERONET and the two model simulations at each site. On each AERONET volume distribution, the standard deviation of each particle size bin is indicated. In addition to the volume distributions, the mean total AOT, coarse mode AOT, and the coarse mode volume median diameter (retrieved in AERONET, from the dust mode in the model) are shown for the AERONET observations and the GEOS-4 GOCART and DEAD simulations, as well as the number of days used to determine the

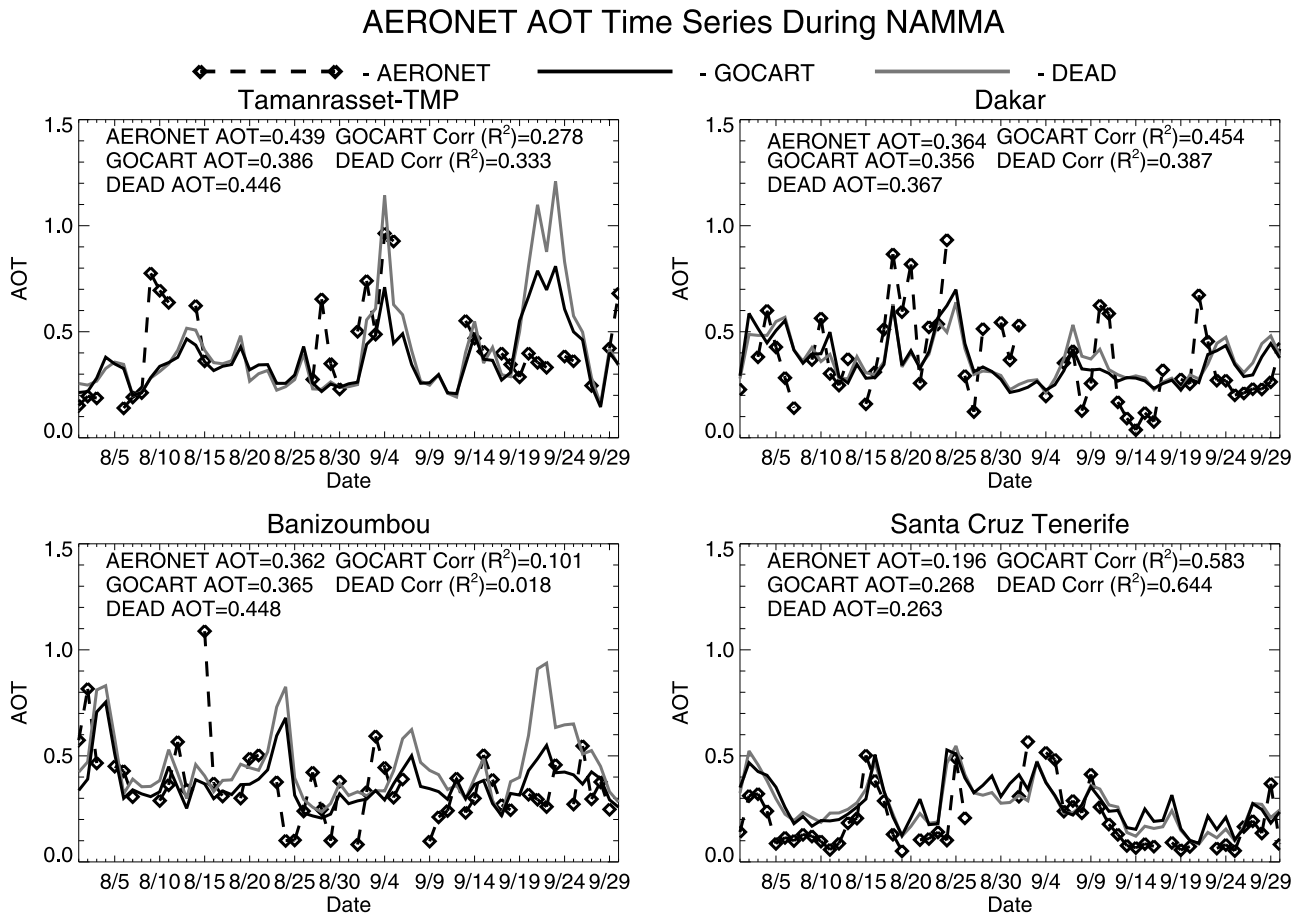

Figure 6. AERONET AOT (dashed-diamond), GEOS-4 GOCART AOT (solid black), and GEOS-4 DEAD AOT (solid gray) during August and September. Mean AOT values and coefficients of determination are displayed in the top left and right, respectively.

averages. At Tamanrasset-TMP only one day was available, and we see that both simulations underestimate the AOT, and hence the overall particle volume. Additionally, the simulations underestimate the relative contribution of large particles to the overall volume, and the model coarse mode median diameter is underestimated relative to the AERONET retrieval. Because there is only one valid day during our time of interest, it is difficult to tell if this large discrepancy between the AERONET and GEOS-4 volume distributions is a common occurrence. Moving away from the source region to the Santa Cruz Tenerife, Dakar, and Banizoumbou sites, we find that there is better agreement between simulated and AERONET coarse-mode distributions. Because of their location downwind of the dust source region, we see narrower AERONET distributions and smaller AERONET coarse mode median diameters (at Dakar and Santa Cruz) as larger particles sediment preferentially from the dust plume, although the model coarse mode median diameters do not exhibit much variability from one site to the other, which could indicate that the simulated removal processes are not reflective of the regional atmospheric environment. In the submicron range, AERONET volume distributions have a second mode that is not seen in the simulated volume distributions, but this feature is due to the presence of nondust aerosols that are not being considered here. Additionally, we see a greater number of submicron particles in the DEAD volume distributions when compared to the GOCART volume distributions, a feature consistent with section 4.1. At all three sites, the AERONET volume distributions peak near 4 μm. Both emission schemes have comparable coarse mode volume median diameters, yet the DEAD volume distributions consistently result in larger median diameters that are more comparable to AERONET.

4.3.2. Airborne in Situ: Langley Aerosol Research Group Experiment

[37] The Langley Aerosol Research Group Experiment (LARGE) recorded in situ measurements of both particle microphysical and optical properties aboard the NASA DC-8 aircraft during the NAMMA field campaign. Sample air was drawn to the instruments through a forward facing, isokinetic inlet probe that was mounted on a window plate located just ahead of the aircraft starboard wing. The sampling inlet had a 50% transmission efficiency at 4 μm in dry diameter and was shown to efficiently transmit both dust and sea salt particles at smaller diameters [*Huebert et al.*, 2004; *McNaughton et al.*, 2007]. At diameters larger than 4 μm, the sampling inlet rejected less than 2% of the particle number concentration (provided by G. Chen et al., unpublished data, 2009). Particle size distributions were determined using a Droplet Measurement Technologies Ultra High Sensitivity Aerosol Spectrometer (UHSAS) for the 0.1–0.7 μm diameter range and a TSI Aerodynamic

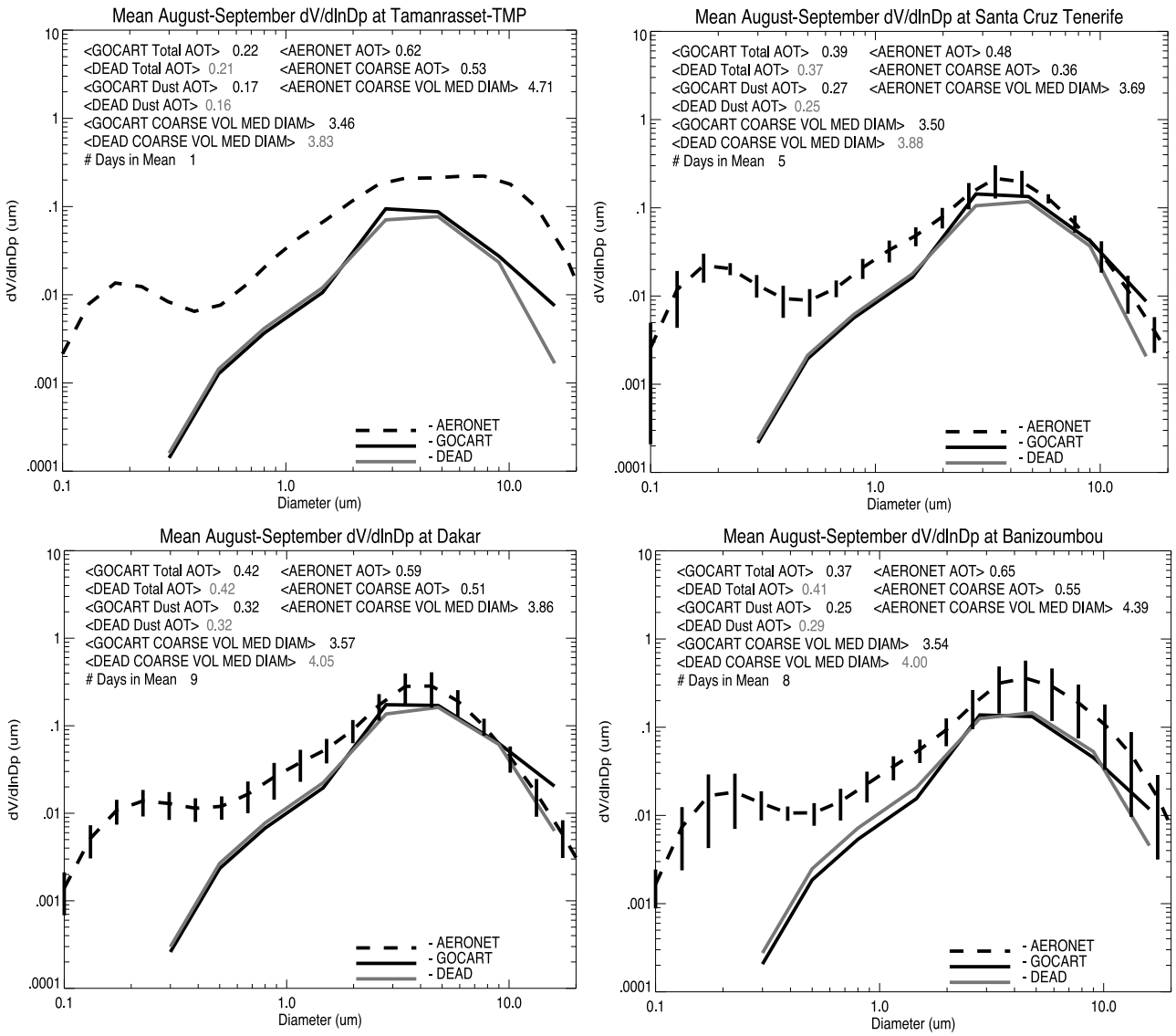

Figure 7. Mean August–September AERONET (dashed), GEOS-4 GOCART (solid black), and GEOS-4 DEAD (solid gray) size distributions.

Particle Sizer (APS) for the 0.7–10 μm range (G. Chen et al., unpublished data, 2009). Both instruments were calibrated using latex spheres. The APS mass-based sizes were converted to geometric diameters using the procedures described by G. Chen et al. (unpublished data, 2009). The observed dust size distributions exhibited a bimodal structure that was fitted with a two lognormal curves to produce the smoothly varying size distributions. For our analysis, we compare our simulated volume distributions to 28 in situ volume distributions at varying altitudes and locations during NAMMA.

[38] Figure 8 shows volume distributions from LARGE and both GEOS-4 simulations (dust-only) on 19 and 26 August 2006. On each day, we show the locations of the sampled distributions along the DC-8 track and their proximity to the MODIS-Aqua and GOCART AOT. Additionally, we show the mean fitted distribution as well as the range of distributions possible based on the standard deviations of the fitted size parameters for a range of altitudes (1.5–2.25, 2.25–3, and 3–3.75 km). On 19 August 2006, while descending into a dust plume, several volume distributions were collected over the tropical North Atlantic Ocean in the area of 14–16.5°N, 21–27°W. With increasing altitude, the in situ volume distributions become narrower as the number of large particles decrease with altitude. Both GEOS-4 distributions exhibit little variability in the vertical, hinting once again that the removal processes may be too relaxed in the model. Additionally, in contrast to the comparison to AERONET, both simulations have peak volumes at larger diameters ($D \sim 4$ μm) than the measurements ($D \sim 2$ μm). Because only the dust contribution to the total volume distribution is compared to the LARGE data, it is not surprising that both simulations do poorly in the submicron range. However, a significant discrepancy exists between all LARGE distributions and the simulated distributions in the range of $1 < D < 2$ μm, where the DEAD scheme is only marginally better. On 25 August 2006, in situ volume distributions were collected during aircraft ascent in the

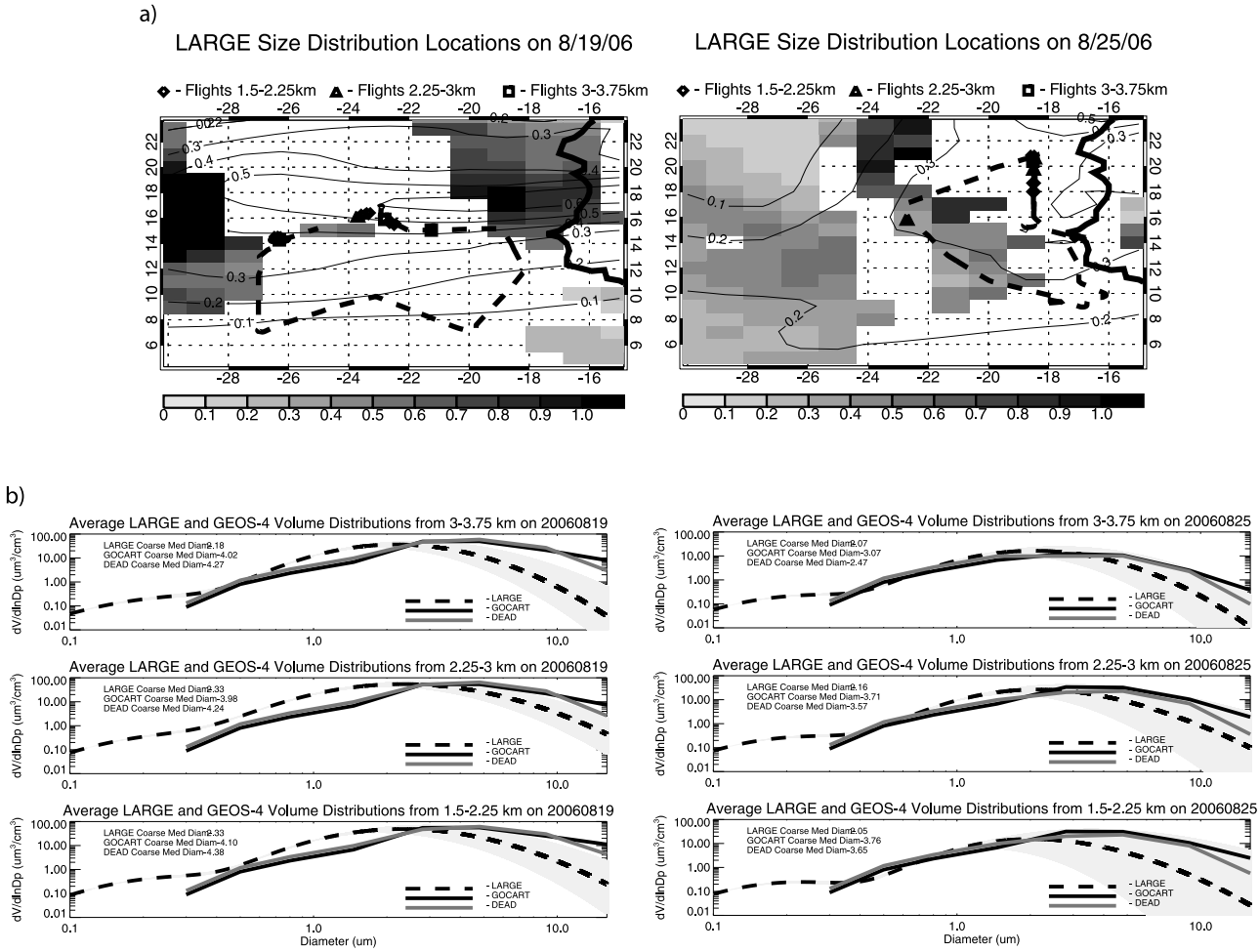

Figure 8. (a) In situ volume distribution locations along the NASA DC-8 track (dashed line) over daily averaged MODIS (shaded) and GOCART (contoured) AOT on 19 August 2006 and 25 August 2006. Mean in situ (dashed), GOCART (solid black), and DEAD (solid gray) volume distributions as a function of altitude on (b) 19 August 2006 and 25 August 2006.

vicinity of 18.5–20°N, 18.5–23°W. On this day, both model simulations better capture the variations in particle size with altitude and show an improved agreement with the airborne measurements in the 1 μm < D < 2 μm diameter range, but exhibit modal diameters that are about 2 μm greater than seen in the LARGE distributions. We note that the in situ measurements are not corrected for hygroscopic growth or for losses within the sample inlet, possibly accounting for a part if not all of the observed differences in the coarse mode size range.

4.4. Aerosol Vertical Profiles

[39] We evaluated the model dust vertical profile in the context of space-based (CALIPSO) and airborne (LASE) lidar observations made during the NAMMA experiment. The horizontal distribution of aerosols is additionally considered in the context of correlated aerosol observations from the MODIS-Aqua and OMI satellite sensors. We note that the CALIPSO, MODIS-Aqua, and OMI observations are near coincident in time, with all three instruments operating on separate satellites flying within a coordinated satellite constellation (the so-called A-Train). Here we consider four case studies where the satellite and airborne observations are correlated.

4.4.1. Data Sets

4.4.1.1. LASE

[40] The Lidar Atmospheric Sensing Experiment (LASE) flew on board the NASA DC-8 aircraft as part of NAMMA, measuring vertical profiles of aerosol and water vapor, operating in the 815 nm region [*Browell et al.*, 2005]. LASE measurements of aerosol scattering ratio are derived by correcting for a small amount of extinction due to water vapor absorption at the relatively nonabsorbing, off-line, wavelength; and aerosol extinction corrected scattering ratio profiles and aerosol extinction profiles are retrieved by using the lidar extinction-to-backscattering ratio values for the aerosol layers from other measurements or using layer aerosol extinction measurements, where available, from LASE [*Ferrare et al.*, 2000a, 2000b; *Ismail et al.*, 2010]. Nominal aerosol scattering and extinction ratios are derived with a vertical resolution of 60 m and horizontal resolution of 2.1 km. LASE operated during all 13 NAMMA flights and obtained aerosol measurements where cloud attenuation effects were not significant. LASE aerosol extinction pro-

files have been shown to have very good agreement with aerosol extinction profiles derived from simultaneous in situ LARGE data [*Ismail et al.*, 2010]. A detailed summary of LASE measurements during NAMMA is given by *Ismail et al.* [2008, 2010].

4.4.1.2. Cloud-Aerosol Lidar With Orthogonal Polarization

[41] The two-channel Cloud-Aerosol Lidar with Orthogonal Polarization (CALIOP) was launched as part of the NASA A-Train on board CALIPSO on 28 April 2006, providing vertical measurements of total attenuated backscatter at a frequency of 20.16 Hz at 532 and 1064 nm [*Vaughan et al.*, 2005]. CALIOP vertical resolution ranges from 60 m in the upper atmosphere to 30 m in the troposphere. At 532 nm, CALIOP sends out linearly polarized light beams and is equipped with receivers that measure parallel and perpendicular components of back-scattered light. Spherical aerosols, such as smoke, and liquid clouds do not strongly depolarize the back-scattered radiation, so they are detected in the parallel detection channel (i.e., the same polarization is detected that is emitted). Because dust is nonspherical, the back-scattered radiation is polarized into both the perpendicular and parallel planes. Thus, the ratio of the perpendicular to parallel back-scattered radiation or depolarization ratio, is high in the presence of dust aerosols and can be used to distinguish dust from spherical aerosols. CALIOP uses the cloud aerosol discrimination (CAD) algorithm to distinguish clouds from aerosol layers. The CAD utilizes the statistical differences in scattering characteristics of clouds and aerosols by computing a lidar color ratio ($\chi = \beta_{1064\ \mathrm{nm}}/\beta_{532\ \mathrm{nm}}$) [*Vaughan et al.*, 2005]. Total attenuated backscatter varies spectrally for aerosols and not for clouds, thus clouds are identified for color ratios equal to one. Because of noisiness in the CALIOP total attenuated backscatter values during daytime overpass (1:30 P.M. local time), only nighttime (1:30 A.M. local time) data are presented.

4.4.1.3. MODIS

[42] A version of the MODIS was launched as part of the NASA A-Train on board the Aqua spacecraft on 4 May 2002. MODIS takes multispectral observations of the atmosphere and retrieves aerosol properties at $10 \times 10\ \mathrm{km}^2$ using two algorithms. The ocean algorithm uses retrievals of radiances from six channels (550, 660, 870, 1240, 1630, and 2130 nm) to derive several aerosol products at seven wavelengths (550–2130 nm and a model fit at 470 nm) [*Remer et al.*, 2005]. The land algorithm uses an empirical relationship from two visible channels (470 and 660 nm) and one near-IR channel (2130 nm) to provide aerosol retrievals at 470, 550, and 660 nm [*Remer et al.*, 2005]. One major disadvantage of using the MODIS aerosol product over land is the inability to sense over bright surfaces, such as deserts. Over the ocean, MODIS does not have this difficulty and can provide reliable measurements of AOT that can be used to track dust transport off the coast of Africa.

4.4.1.4. Ozone Monitoring Instrument

[43] The Ozone Monitoring Instrument (OMI) was launched as part of the A-Train on board Aura on 15 July 2004, providing aerosol retrievals at 354 and 388 nm with a nadir horizontal resolution of $13 \times 24\ \mathrm{km}^2$ [*Torres et al.*, 2007]. The use of UV aerosol retrievals allows for OMI to easily distinguish dust aerosols from both land and ocean surface, which are both "dark" at UV wavelengths. Thus, unlike MODIS, OMI is able to provide aerosol retrievals over desert regions. OMI calculates a UV aerosol index (AI) at 354 nm using retrievals at 354 and 388 nm. AI values are sensitive to aerosols with a spectrally varying absorbing index of refraction and are positive for absorbing aerosols, such as dust.

4.4.2. Case Studies

[44] For our comparison to NAMMA observations, we chose to discuss two case studies. The DC-8 flight on 26 August 2006 (Figure 9) is representative of other NAMMA flights, as observations are made over the ocean under similar synoptic conditions. The DC-8 flight on 5 September 2006 (Figure 10) is unique as the DC-8 aircraft made way over the African continent. For each NAMMA flight presented, the DC-8 track is shown in the top left plot by the black line. The square marks the beginning of the flight and an "X" marks the end. In addition to the flight track, LASE extinction (815 nm) is compared to sampled GEOS-4 GOCART and DEAD extinction from all aerosols (815 nm) in the left column. GEOS-4 grid cells were sampled at the nearest model synoptic time along the DC-8 track. The DC-8 altitude is indicated in the LASE and GEOS-4 curtain plots with a solid black line. Also shown on the top left plot is the CALIOP nighttime pass (solid red line) that is nearest the DC-8 flight track. The beginning of each CALIOP track is marked by a square and the end is marked by an X. In each center column, CALIOP total attenuated backscatter (532 nm), CALIOP depolarization ratio (532 nm), GEOS-4 GOCART from all aerosols extinction (532 nm), and GEOS-4 DEAD extinction from all aerosols (532 nm) are shown. Both GEOS-4 simulations are sampled along the CALIPSO track similar to the DC-8 sampling. In the right column, OMI aerosol index (354 nm), MODIS-Aqua AOT (550 nm), GEOS-4 GOCART AOT from all aerosols (550 nm), and GEOS-4 DEAD AOT from all aerosols (550 nm) are plotted to identify spatial distributions of observed and simulated dust plumes.

4.4.2.1. 26 August 2006

[45] At 1300Z on 26 August 2006, the NASA DC-8 encountered an intense low-level dust plume (Figure 9). The aircraft ascended to 10.5 km as it headed in a northwest direction. Upon reaching 20°N, the aircraft maintained a steady altitude of 10.5 km and changed course to follow a counterclockwise path above a low-level dust plume over the tropical North Atlantic Ocean. Near 18°N, the aircraft briefly dipped down to 7 km but quickly ascended to 11 km for the second half of the flight before returning to Capo Verde.

[46] On this day, simulated extinction profiles from both emission schemes are nearly identical. Both GEOS-4 simulations are very similar and match well with LASE extinction beneath 4 km. Above 4 km, model extinction values continue to be high up to 6 km, where LASE is generally capped at 4 km. While CALIOP appears to show an elevated dust plume on its transit, both instances of the model show a dust layer that extends to the surface and situated somewhat more to the south. On the other hand, the peak AOT in the model appears to be near the surface and coincident with marine stratus clouds CALIOP observations (high backscatter and modest depolarization below about

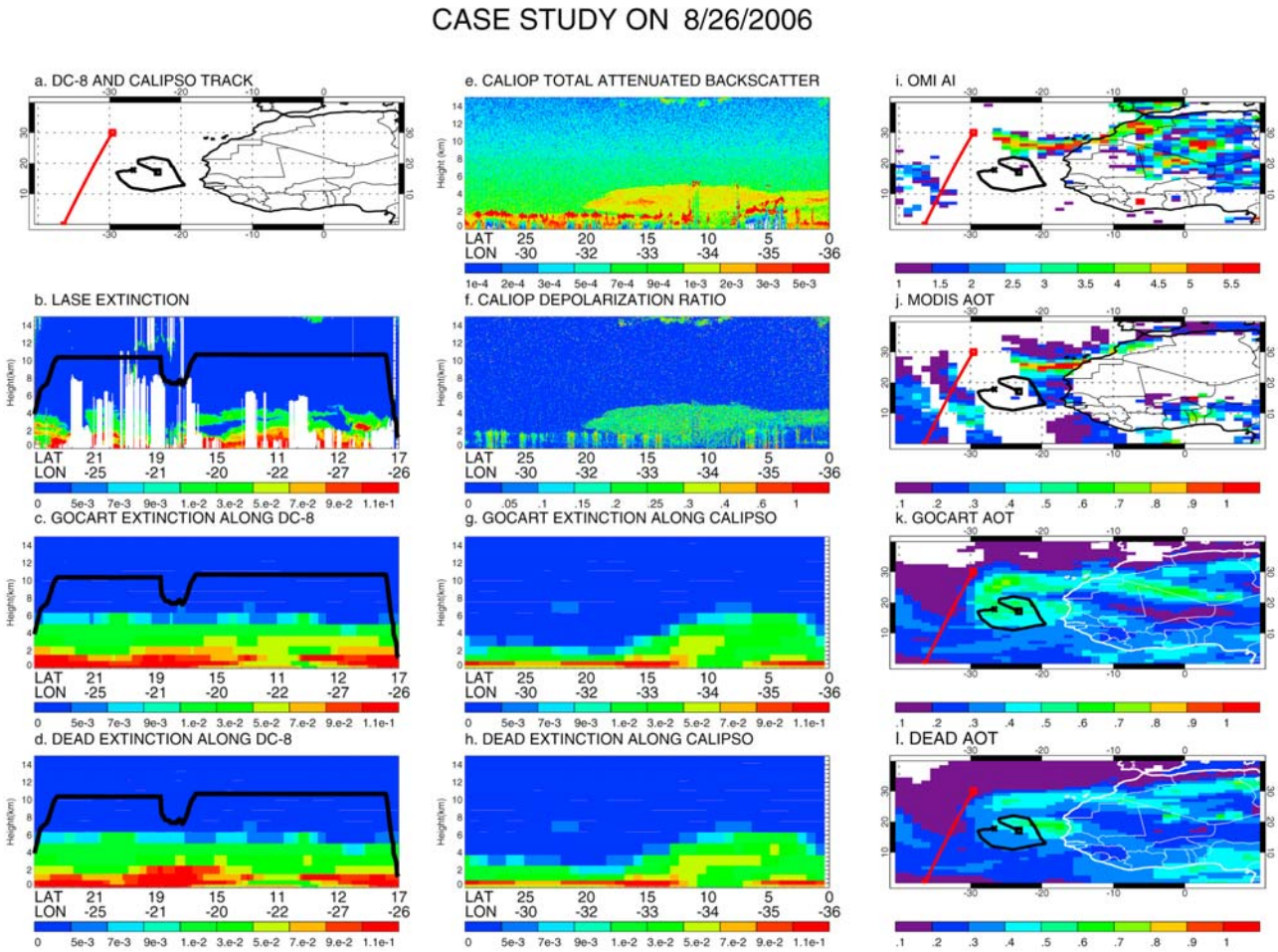

Figure 9. NASA DC-8 (black) and CALIPSO (red) (a) tracks, (b) LASE extinction, (c) GEOS-4 DC-8 sampled GOCART extinction, (d) GEOS-4 DC-8 sampled DEAD extinction, (e) CALIOP total attenuated backscatter, (f) CALIOP depolarization ratio, (g) GEOS-4 CALIPSO sampled GOCART extinction, (h) GEOS-4 CALIPSO sampled DEAD extinction, (i) OMI Aerosol Index, (j) MODIS-Aqua AOT, (k) GEOS-4 GOCART AOT, and (l) GEOS-4 DEAD AOT on 26 August 2006.

2 km altitude extending along the northern portion of the transit), indicating that the model is able to capture swelling by hygroscopic aerosols within the humid marine environment. Although the OMI and MODIS observations are not time coincident with the CALIOP data and apparently miss the DC-8 flight on this day, both instances of the model place dust plumes consistently with their observations over North Africa and the Canary Islands, but underestimate the AOT.

4.4.2.2. 5 September 2006

[47] On 5 September 2006, the NASA DC-8 began a flight at 1200Z (Figure 10). During the flight, the aircraft increased altitude to a steady 11 km as it flew northeast to 19°N and then maintained constant latitude as it flew over the continent to 10°W over an intense dust plume. The aircraft then spiraled down into the dust plume to 1 km, then turned around and followed the same path back Capo Verde while slowly ascending to 8 km. This flight is unique because it is one of the few NAMMA flights that were conducted over land.

[48] On this day, both schemes have excellent agreement with the LASE extinction profile. Unlike the previous case study illustrated, both emission schemes transport dust to altitudes comparable to those retrieved by LASE. CALIOP total attenuated backscatter and depolarization ratio show a strong elevated dust plume extending from 30°N to 10°N. We note that the strong backscatter signals seen above 5 km are indicative of ice clouds due to their high altitude, heterogeneous structure, polarization of the backscatter signal at the feature altitude, and complete attenuation below. These clouds are not shown in the model results. Both schemes capture the elevation and latitudinal extent of the dust plume observed by CALIOP. OMI AI and MODIS AOT show dust plumes over northern Africa and off the coast of Mauritania. Both simulated plumes are positions slightly to the north and east of each observed plume. MODIS tropical North Atlantic AOT spatial distributions and magnitudes are comparable to both schemes.

5. Summary and Conclusions

[49] In this paper, we present a comparison of simulated dust distributions to several observation data sets obtained during the NAMMA field experiment. The simulations were

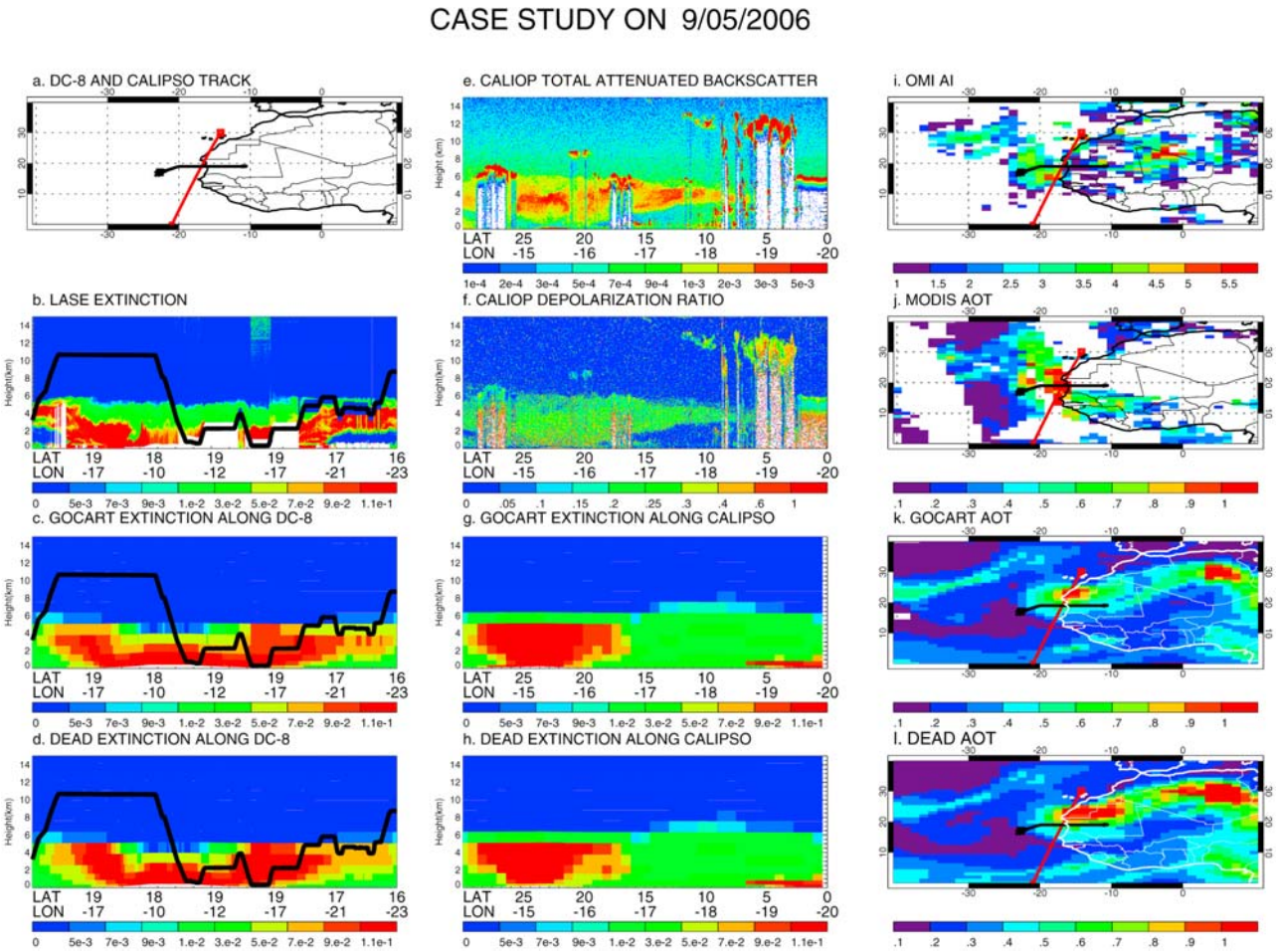

Figure 10. NASA DC-8 (black) and CALIPSO (red) (a) tracks, (b) LASE extinction, (c) GEOS-4 DC-8 sampled GOCART extinction, (d) GEOS-4 DC-8 sampled DEAD extinction, (e) CALIOP total attenuated backscatter, (f) CALIOP depolarization ratio, (g) GEOS-4 CALIPSO sampled GOCART extinction, (h) GEOS-4 CALIPSO sampled DEAD extinction, (i) OMI Aerosol Index, (j) MODIS-Aqua AOT, (k) GEOS-4 GOCART AOT, and (l) GEOS-4 DEAD AOT on 5 September 2006.

conducted with two different dust aerosol emission schemes. Both schemes used the same source function map to locate dust source regions but differed in their underlying parameterization of the emission process. The emission schemes were tuned so that the regionally averaged dust AOT over North Africa during the August–September 2006 period was the same for each.

[50] The impact of the emission scheme choice is most clearly seen in the mass distributions of emitted dust. The GOCART scheme more broadly distributes emission over the source region, whereas the emissions in the DEAD scheme are more localized (Figure 2). We attribute this difference to differences in how the dust emission wind speed threshold is used in each parameterization. In the DEAD scheme, emissions are driven by wind friction speed, which is comparable in magnitude to the wind speed threshold for emissions, and so emissions are more episodic. In contrast, the GOCART scheme drives emissions by the 10 m wind speed, which is typically an order of magnitude greater than the threshold wind speed, and so the wind speed threshold is more frequently exceeded throughout the domain. Additionally, although the two schemes were tuned to yield the same regional AOT values, differences in the choice of emitted particle size distribution result in different emission magnitudes (91 Tg/month for GOCART scheme versus 54 Tg/month for DEAD scheme). More mass in the GOCART scheme is emitted into larger particle sizes that have shorter residence times because of removal by gravitational settling, while the DEAD scheme has relatively more mass emitted into smaller, more optically efficient particles and fewer large particles (Figure 3). Despite these differences in the emitted particle size distribution, both schemes evolve similar particle distributions during transport (Figures 7 and 8). Comparing simulated particle size distributions to AERONET measurements (Figure 7), we found poor agreement between the simulated and retrieved distributions near the source region (Tamanrasset-TMP), and we did not accurately capture the observed relationship between smaller particle sizes and the coarse mode with distance downwind of the source regions. The DEAD scheme had somewhat larger coarse mode median diameters, which agreed slightly better with AERONET. In general, both

schemes maintained fairly constant particle size distributions during transport.

[51] Comparisons of GOCART and DEAD AOT values to observations from MISR (Figure 4) show that both schemes produce similar spatial distributions of dust downwind of source regions, but different distributions over the source region. The implication is that while the downwind distributions may evolve similarly in both schemes, the radiative forcing due to the dust over the source region might be quite different. This will be explored further in the next generation, GEOS-5 modeling system [*Rienecker et al.*, 2008], which includes now the capability for online radiative transfer calculations and feedback of the simulated aerosols on the model climate.

[52] In comparison to AERONET AOT observations (Figure 6), the GOCART and DEAD AOT are highly correlated with each other in time, but differ somewhat in magnitude, especially during high AOT events, which is not inconsistent with the MISR observations discussed above. Both MISR and AERONET show that neither emission scheme performs, especially well over the source region at capturing specific events. To the south of the source region, daily AERONET AOT correlations with each scheme are also poor, but MISR monthly mean AOT values are comparable. This suggests that the timing of specific dust transport episodes to the south of the source region may not be correct, but the averaged pattern is comparable to the observations. Both schemes have their best agreement with MISR and AERONET AOT farther downwind of the source region (Santa Cruz, Tenerife) and over the tropical North Atlantic Ocean. This suggests that the meteorology over the source regions may not be sufficiently accurate to capture specific dust lifting events, but that once dust is entrained in the large-scale flow downwind of sources the model is adequate to resolving dust transport episodes. This result is consistent with *Colarco et al.* [2003], who showed that the timing of dust events is more sensitive to transport dynamics rather than the dust model chosen.

[53] We compared the simulated vertical profiles from both schemes to NAMMA airborne observations and space-based CALIOP observations for two cases. To our knowledge, this is the first time that dust vertical distribution has been explored particular in the same model running with different dust emission schemes. In both cases, the model did a reasonable job of placing the dust plumes from Africa over the tropical north Atlantic, and in general there was no apparent difference in the vertical plume placement between the schemes. In one of the cases examined (26 August, Figure 9), although the model had located the main dust plume correctly below 4 km altitude, there was considerable transport of dust at higher altitudes as well. There are well-known issues of excessive vertical diffusion in numerical transport models that result from limited vertical resolution. Further sensitivity studies will be required to isolate that possible cause from errors in the vertical mixing by dry convection over the source region or even long-range transport of dust from distant source regions as explanations for simulated dust at too high an altitude.

[54] We have shown that the GOCART and DEAD emission schemes produce similar AOT distributions during the timeframe of the NAMMA field experiment. From a physical standpoint, the DEAD emission scheme poses a more realistic representation of dust emission by correctly comparing the surface friction speed to the threshold speed and simulating particle saltation. However, emitted dust distributions are dependent on several unknowns such as soil particle size distributions, soil clay content, and model assumptions that are used to compute the surface friction speed. Additionally, the 10 m wind speed used by the GOCART scheme to parameterize dust emission is typically known to higher degree of accuracy and global availability than surface friction speed. This is significant over a poorly observed region such as the Sahara Desert, as small errors in the surface friction speed can have a large impact on simulated dust emissions.

[55] Despite the differences in the emission schemes, both simulations become more comparable to observations with distance from the source region. Because observations are limited within the source region and dust production is subject to the accuracy of the assimilated meteorology, it is not surprising that the largest discrepancies exist in this region. Additionally, the use of instantaneous grid-cell averaged winds every 6 h to parameterize the emission process is not likely to provide sufficient spatial and temporal resolution to capture the effects of wind gusts, a key control on dust production. Therefore, for our set of model simulations, we determine that errors in the simulated meteorology are likely more significant than the differences between the emission schemes. However, future representation of sub-grid and temporal wind variability into the emission process may help with the timing of dust events and differentiate the emissions schemes over the source region. From our analysis of observed and simulated dust distributions, emission scheme choice makes a small difference when considering the particle size distributions of the load. On the basis of the available AERONET and airborne in situ size distributions during the NAMMA experiment, the fixed particle size distribution chosen for the DEAD scheme produces a particle size distribution that is slightly more comparable to observations. Using optical measurements over North Africa during the NAMMA experiment, we were unable to find significant advantages or disadvantages of using either scheme. However, the significant difference in emitted particle size distributions and corresponding mass between the emission schemes over the source region may be useful to identify which scheme is more preferable for global model use if there are sufficient observations of mass concentrations during NAMMA. Additionally, while changing our region or time period of interest may help to differentiate the schemes, we suspect that the most significant difference will be seen if the model resolution is increased. We expect if the microscale processes and meteorology that control dust emission are better resolved, there will be a large effect on simulated emitted dust distributions owing to the subtle differences of the emission schemes. We will explore this further in the next generation GEOS-5 modeling system.

[56] **Acknowledgments.** We would like to thank Brent Holben and Didier Tanré, Emilio Cuevas, and Juan Cuesta for their efforts in establishing and maintaining the Dakar, Banizoumbou, Santa Cruz Tenerife, and Tamanrasset-TMP AERONET sites. We also thank Arlindo da Silva for his support in the NASA GEOS-4 modeling initiative. This work was funded by the NASA Modeling, Analysis, and Prediction program and a NASA Earth System Science Fellowship.

References

Abdou, W. A., D. J. Diner, J. V. Martonchik, C. J. Bruegge, R. A. Kahn, B. J. Gaitley, K. A. Crean, L. A. Remer, and B. Holben (2005), Comparison of coincident MISR and MODIS aerosol optical depths over land and ocean scenes containing AERONET sites, *J. Geophys. Res.*, *110*, D02109, doi:10.1029/2008JD010754.

Alley, R., et al. (2007), *Climate Change 2007: The Physical Science Basis, Summary for Policymakers*, IPCC Secretariat, World Meteorol. Organ., Geneva, Switzerland.

Bloom, S., et al. (2005), Documentation and validation of the Goddard Earth Observing System (GEOS) data assimilation system—version 4, *Tech. Memo. 104606*, in *Technical Report Series on Global Modeling and Data Assimilation*, vol. 26, NASA Goddard Space Flight Cent., Greenbelt, Md.

Bonan, G. B., K. W. Oleson, M. Vertenstein, S. Levis, X. B. Zeng, Y. J. Dai, R. E. Dickinson, and Z. L. Yang (2002), The land surface climatology of the Community Land Model coupled to the NCAR Community Climate Model, *J. Clim.*, *15*, 3123–3149.

Browell, E. V., W. B. Grant, and S. Ismail (2005), Airborne lidar systems, in *Laser Remote Sensing*, edited by T. Fujii and T. Fukuchi, pp. 723–779, Taylor and Francis, New York.

Cakmur, R. V., et al. (2006), Constraining the magnitude of the global dust cycle by minimizing the difference between model and observations, *J. Geophys. Res.*, *111*, D06207, doi:10.1029/2005JD005791.

Carlson, T. N., and J. M. Prospero (1972), The large-scale movement of Saharan air outbreaks over the northern equatorial Atlantic, *J. Appl. Meteorol.*, *11*, 283–297.

Chin, M., et al. (2002), Tropospheric aerosol optical thickness from the GOCART model and comparisons with satellite and Sun photometer measurements, *J. Atmos. Sci.*, *59*(3), 461–483.

Clarke, A., et al. (2007), Biomass burning and pollution aerosol over North America: Organic components and their influence on spectral optical properties and humidification response, *J. Geophys. Res.*, *112*, D12S18, doi:10.1029/2006JD007777.

Colarco, P. R., O. B. Toon, and B. N. Holben (2003), Saharan dust transport to the Caribbean during PRIDE: 1. Influence of dust sources and removal mechanisms on the timing and magnitude of downwind aerosol optical depth events from simulations of in situ and remote sensing observations, *J. Geophys. Res.*, *108*(D19), 8589, doi:10.1029/2002JD002658.

D'Almeida, G. A. (1987), On the variability of desert aerosol radiative characteristics, *J. Geophys. Res.*, *92*(D3), 3017–3026.

DeFries, R. S., and J. R. G. Townshend (1994), NDVI-Derived land-cover classifications at a global-scale, *Int. J. Remote Sens.*, *15*(17), 3567–3586.

DeMott, P. J., K. Sassen, M. R. Poellot, D. Baumgardner, D. C. Rogers, S. D. Brooks, A. J. Prenni, and S. M. Kreidenweis (2003), African dust aerosols as atmospheric ice nuclei, *Geophys. Res. Lett.*, *30*(14), 1732, doi:10.1029/2003GL017410.

Diner, D. J., et al. (1998), Multi-angle Imaging SpectroRadiometer (MISR)—Instrument description and experiment overview, *IEEE Trans. Geosci. Remote Sens.*, *36*(4), 1072–1087, doi:10.1109/36.700992.

Dubovik, O., and M. D. King (2000), A flexible inversion algorithm for retrieval of aerosol optical properties from Sun and sky radiance measurements, *J. Geophys. Res.*, *105*(D16), 20,673–20,696.

Falkowski, P. G., R. T. Barber, and V. Smetacek (1998), Biogeochemical controls and feedbacks on primary production, *Science*, *281*, 200–206.

Fécan, F., B. Marticorena, and G. Bergametti (1999), Parameterization of the increase of the aeolian erosion threshold wind friction velocity due to soil moisture for arid and semi-arid areas, *Ann. Geophys.*, *17*(1), 149–157.

Ferrare, R. A., et al. (2000a), Comparison of aerosol optical properties and water vapor among ground and airborne lidars and Sun photometers during TARFOX, *J. Geophys. Res.*, *105*(D8), 9917–9933.

Ferrare, R. A., et al. (2000b), Comparison of LASE, aircraft, and satellite measurements of aerosol optical properties and water vapor during TARFOX, *J. Geophys. Res.*, *105*(D8), 9935–9947.

Gillette, D. A., B. Marticorena, and G. Bergametti (1998), Change in the aerodynamic roughness height by saltating grains: Experiments assessment, test of theory, and operational parameterization, *J. Geophys. Res.*, *103*(D6), 6203–6209.

Ginoux, P., M. Chin, I. Tegen, J. M. Prospero, B. Holben, O. Dubovik, and S.-J. Lin (2001), Sources and distributions of dust aerosols simulated with the GOCART model, *J. Geophys. Res.*, *106*(D17), 20,255–20,273.

Gomes, L., G. Bergametti, G. Coudé-Gaussen, and P. Rognon (1990), Submicron desert dusts: A sandblasting process, *J. Geophys. Res.*, *95*(D9), 13,927–13,935.

Grini, A., and C. S. Zender (2004), Roles of saltation, sandblasting, and wind speed variability on mineral dust aerosol size distribution during the Puerto Rican Dust Experiment (PRIDE), *J. Geophys. Res.*, *109*, D07202, doi:10.1029/2003JD004233.

Hillel, D. (1982), *Introduction to Soil Physics*, Academic, San Diego, Calif.

Holben, B. N., et al. (2001), An emerging ground-based aerosol climatology: Aerosol optical depth from AERONET, *J. Geophys. Res.*, *106*(D11), 12,067–12,097.

Huebert, B. J., et al. (2004), PELTI: Measuring the passing efficiency of an airborne low turbulence aerosol inlet, *Aerosol Sci. Technol.*, *38*, 803–826, doi:10.1080/027868290500823.

Ismail, S., et al. (2008), LASE measurements of water vapor, aerosol, and cloud distributions in Saharan air layers and tropical disturbances, paper presented at the 24th International Laser Radar Conference, Int. Coord. Group for Laser Atmos. Stud., Boulder, Colo., 21–26 July.

Ismail, S., et al. (2010), LASE measurements of water vapor, aerosol, and cloud distributions in Saharan air layers and tropical disturbances, *J. Atmos. Sci.*, in press.

Ivesen, J. D., and B. R. White (1982), Saltation threshold on Earth, Mars, and Venus, *Sedimentology*, *29*(1), 111–119.

Jickells, T. D., et al. (2005), Global iron connections between desert dust, ocean biogeochemistry, and climate, *Science*, *308*(5718), 67–71.

Kahn, R., et al. (2005), MISR calibration and implications for low-light-level aerosol retrieval over dark water, *J. Atmos. Sci.*, *62*(4), 1032–1052.

Karyampudi, V. M., et al. (1999), Validation of the Saharan dust plume conceptual model using lidar, Meteosat, and ECMWF data, *Bull. Am. Meteorol. Soc.*, *80*, 1045–1075.

Kiehl, J. T., J. J. Hack, G. B. Bonan, B. A. Boville, B. P. Briegleb, D. L. Williamson, and P. J. Rasch (1996), Description of the NCAR Community Climate Model (CCM3), *NCAR Tech. Note NCAR/TN-420+STR*, 152 pp., Natl. Cent. for Atmos. Res., Boulder, Colo.

Köpke, P., M. Hess, I. Schult, and E. P. Shettle (1997), The Global Aerosol Data Set (GADS), *MPI-Rep.*, *243*, 44 pp., Max-Planck-Inst., Hamburg, Germany.

Lin, S.-J. (2004), A vertically Lagrangian finite-volume dynamical core for global models, *Mon. Weather Rev.*, *132*, 2293–2307.

Luo, C., N. M. Mahowald, and J. del Corral (2003), Sensitivity study of meteorological parameters on mineral aerosol mobilization, transport, and distribution, *J. Geophys. Res.*, *108*(D15), 4447, doi:10.1029/2003JD003483.

Mahowald, N. M., and C. Luo (2003), A less dusty future?, *Geophys. Res. Lett.*, *30*(17), 1903, doi:10.1029/2003GL017880.

Marticorena, B., and G. Bergametti (1995), Modeling the atmospheric dust cycle: 1. Design of a soil-derived dust emission scheme, *J. Geophys. Res.*, *100*(D8), 16,415–16,430.

McNaughton, C. S., et al. (2007), Results from the DC-8 Inlet Characterization Experiment (DICE): Airborne versus surface sampling of mineral dust and sea salt aerosols, *Aerosol Sci. Techonol.*, *41*(2), 136, doi:10.1080/02786820601118406.

Prospero, J. M., P. Ginoux, O. Torres, S. E. Nicholson, and T. E. Gill (2002), Environmental characterization of global sources of atmospheric soil dust identified with the Nimbus 7 Total Ozone Mapping Spectrometer (TOMS) absorbing aerosol product, *Rev. Geophys.*, *40*(1), 1002, doi:10.1029/2000RG000095.

Remer, L. A., et al. (2005), The MODIS aerosol algorithm, products, and validation, *J. Atmos. Sci.*, *62*(4), 947–973.

Rienecker, M. M., et al. (2008), The GEOS-5 Data Assimilation System—Documentation of versions 5.0.1, 5.1.0, and 5.2.0.118, *Tech. Rep. Series on Global Model. and Data Assimilation, NASA/TM-2008-104606*, vol. 27, NASA Goddard Space Flight Cent., Greenbelt, Md.

Rosenfeld, D., Y. Rudich, and R. Lahav (2001), Desert dust suppressing precipitation: A possible desertification loop, *Proc. Natl. Acad. Sci.*, *98*(11), 5975–5980.

Shao, Y., and M. R. Raupach (1993), Effect of saltation bombardment on the entrainment of dust by wind, *J. Geophys. Res.*, *98*(D7), 12,719–12,726.

Smirnov, A., B. N. Holben, T. F. Eck, O. Dubovik, and I. Slutsker (2000), Cloud-screening and quality control algorithms for the AERONET database, *Remote Sens. Environ.*, *73*(3), 337–349.

Sokolik, I. N., and O. B. Toon (1996), Direct radiative forcing by anthropogenic airborne mineral aerosols, *Nature*, *381*(6584), 681–683.

Tegen, I., and I. Fung (1994), Modeling of mineral dust in the atmosphere-sources, transport, and optical-thickness, *J. Geophys. Res.*, *99*(D11), 22,897–22,914.

Tegen, I., and A. A. Lacis (1996), Modeling of particle size distribution and its influence on the radiative properties of mineral dust aerosol, *J. Geophys. Res.*, *101*(D14), 19,237–19,244.

Tegen, I., and R. Miller (1998), A general circulation model study on the interannual variability of soil dust aerosol, *J. Geophys. Res.*, *103*(D20), 25,975–25,995.

Torres, O., A. Tanskanen, B. Veihelmann, C. Ahn, R. Braak, P. K. Bhartia, P. Veefkind, and P. Levelt (2007), Aerosols and surface UV products from Ozone Monitoring Instrument observations: An overview, *J. Geophys. Res.*, *112*, D24S47, doi:10.1029/2007JD008809.

Vaughan, M., S. Young, D. Winker, K. Powell, A. Omar, Z. Liu, Y. Hu, and C. Hostetler (2005), Fully automated analysis of space-based lidar data: An overview of the CALIPSO retrieval algorithms and data products, *Proc. SPIE Int. Soc. Opt. Eng.*, *5575*, 16–30.

Wong, S., A. E. Dessler, N. M. Mahowald, P. Yang, and Q. Feng (2009), Maintenance of lower tropospheric temperature inversion in the Saharan air layer by dust and dry anomaly, *J. Clim.*, *22*(19), 5149–5162.

Yoshioka, M., N. M. Mahowald, A. J. Conley, W. D. Collins, D. W. Fillmore, C. S. Zender, and D. B. Coleman (2007), Impact of desert dust radiative forcing on Sahel precipitation: Relative importance of dust compared to sea surface temperature variations, vegetation changes, and greenhouse gas warming, *J. Clim.*, *20*(8), 1445–1467.

Zender, C. S., H. S. Bian, and D. Newman (2003), Mineral Dust Entrainment and Deposition (DEAD) model: Description and 1990s dust climatology, *J. Geophys. Res.*, *108*(D14), 4416, doi:10.1029/2002JD002775.

Zender, C. S., R. Miller, and I. Tegen (2004), Quantifying mineral dust mass budgets: Terminology, constraints, and current estimates, *Eos Trans. AGU*, *85*(48), 509–512.

Zhu, A., V. Ramanathan, F. Li, and D. Kim (2007), Dust plumes over the Pacific, Indian, and Atlantic oceans: Climatology and radiative impact, *J. Geophys. Res.*, *112*, D16208, doi:10.1029/2007JD008427.

B. Anderson, Chemistry and Dynamics Branch/Science Directorate, Mail Stop 483, NASA Langley Research Center, Hampton, VA 23681, USA.

E. Browell, G. Chen, R. Ferrare, and S. Ismail, Mail Stop 401A, NASA Langley Research Center, Hampton, VA 23681, USA.

P. Colarco, Code 613.3, NASA Goddard Space Flight Center, Greenbelt, MD 20771, USA.

E. Nowottnick, Department of Atmospheric and Oceanic Sciences, University of Maryland, Bldg. 224, College Park, MD 20742, USA. (epnowott@atmos.umd.edu)